

UKAEA-CCFE-PR(24)202

Jacob B.J. Chapman, Mark. R. Gilbert, Duc Nguyen-
Manh

Ab-initio investigation into the stability of hydrogen isotopes (protium, deuterium and tritium) in alpha-Fe and dilute Fe-Cr alloys

Enquiries about copyright and reproduction should in the first instance be addressed to the UKAEA Publications Officer, Culham Science Centre, Building K1/O/83 Abingdon, Oxfordshire, OX14 3DB, UK. The United Kingdom Atomic Energy Authority is the copyright holder.

The contents of this document and all other UKAEA Preprints, Reports and Conference Papers are available to view online free at scientific-publications.ukaea.uk/

Ab-initio investigation into the stability of hydrogen isotopes (protium, deuterium and tritium) in alpha-Fe and dilute Fe-Cr alloys

Jacob B.J. Chapman, Mark. R. Gilbert, Duc Nguyen-Manh

Ab initio investigation into the stability of hydrogen isotopes (protium, deuterium and tritium) in α -Fe and dilute FeCr alloys

Jacob B. J. Chapman,^{*} Mark R. Gilbert,[†] and Duc Nguyen-Manh[‡]
United Kingdom Atomic Energy Authority
(Dated: September 24, 2023)

Materials within a viable D-T fusion power-plant will be subject to hydrogen isotope permeation through implantation, adsorption and transmutation. Hydrogen is known to have low solubility in iron but irradiation-induced defects such as vacancies can strongly trap multiple hydrogen atoms. Tritium breeding blankets will be required to compensate for tritium captured by plasma-facing components and waste management strategies must account for tritium retention due its radioactivity. It is common place for theoretical models to use protium as a surrogate for all hydrogen isotopes when investigating microstructural evolution and fatigue mechanisms within fusion engineering considerations. In this work we present a systematic investigation into the relative stability of hydrogen isotopes within body-centred-cubic (bcc) Fe using the density functional theory method with zero-point energy and elastic corrections. We focus on hydrogen interactions in the bulk, trapping in mono-vacancies and adsorption on clean low index surfaces. Hydrogen interactions are further considered with Cr in the dilute limit within the Fe matrix. We show that all hydrogen isotopes are highly mobile in the bulk and reside in tetrahedral interstitials but the diffusivity reduces with mass. Protium migrates via the octahedral site whilst tritium rotates into an adjacent tetrahedral site. The activation barrier for both pathways is degenerate for deuterium which becomes the most mobile isotope at fusion operating temperatures. Hydrogen is repelled by Cr which tends to increase migration barriers by up to 20 meV. Trapping energies of deuterium in a mono-vacancy closely match desorption stages from ion-beam implantation-annealing[1, 2]. The binding of the heavier isotopes is more exothermic than protium. However, dissolution energies between isotopes is typically within 10 meV such that we do not expect practical kinetic isotope effects at operating temperatures. Cr substitutions near a vacancy change the relative incremental binding energies and push hydrogen away from near octahedral sites. The binding energy to a Cr-vacancy complex is lower for 1-3 hydrogen relative to a vacancy in the absence of Cr but is increased as the complex becomes saturated. The binding energy of heavier hydrogen isotopes to both (100) and (110) surfaces are lower than protium. Subsurface Cr is shown to change the preferred hollow adsorption site to a bridge site on a (100) surface, increasing the binding energy by as much as 50%. Finally, we present elastic dipole tensors and relaxation volumes of the hydrogen implanted systems which can be used to represent source terms in continuum models of irradiated materials[3].

I. INTRODUCTION

Hydrogen permeation is known to cause fatigue and ultimately failure of many materials[4–7] with hydrogen embrittlement investigated for over a century[8]. A variety of mechanisms have been proposed to explain hydrogen induced embrittlement and corrosion in structural materials such as steels[7, 9, 10]. Engineering assurances and mitigation strategies can be exploited from atomistic simulations which can identify the mechanisms responsible for the deleterious effects[11–15].

Metallic alloys have transformed society with applications across automotive, aerospace, medical and architectural industries and offers pathways to exciting new technologies such as fusion powerplants[16–18]. Steels in particular can be considered as one of the pillars of modern civilisation along with cement, plastic and ammonia. As of 2021, 1.9 billion tonnes of steel is produced annually accounting for 7% of the global CO₂ emissions[19].

Iron and iron based steel can absorb hydrogen during its production, processing or service. Recent advancements using processes including Direct Reduced Iron are paving the way to decarbonise the steel industry by reacting iron ore directly with hydrogen and water[20]. Understanding how hydrogen accumulates and interacts with lattice defects such as solute or alloying elements[14], surfaces[11, 21, 22], dislocations[23–25], vacancies[26–28] and voids[10, 29] is of fundamental scientific and technological interest to ensure efficient fabrication and safe utilisation of modern steels.

Iron-based alloys attain a myriad of complex magnetic states, such as ferromagnetic, ferrimagnetic, antiferromagnetic, incommensurate spin density waves and spin-glasses. Their mechanical properties are partially governed by the population of these magnetic states [30, 31]. For example, in pure iron, the softening of the tetragonal shear modulus C' near the Curie temperature T_C is driven by magnetism [32–34]. Even the bcc crystal structure of iron owes its stability to the free energy contributions from both lattice and magnetic excitations [35–40]. Magnetism is also responsible for the $\langle 110 \rangle$ dumb-bell being the most stable self interstitial configuration in α -Fe in contrast to other bcc metals [41, 42]. Mag-

^{*} <https://orcid.org/0000-0001-5792-8991>

[†] <https://orcid.org/0000-0001-8935-1744>

[‡] <https://orcid.org/0000-0001-6061-9946>

netic interactions lower the energy of all interstitial configurations, however, non-Heisenberg magnetic interactions in the $\langle 111 \rangle$ configuration add an energy penalty which results in the $\langle 110 \rangle$ and tetrahedral configurations dropping lower in energy than the $\langle 111 \rangle$ dumbbell and crowdion [43]. Magnetic states are significantly changed in the vicinity of dislocations[44, 45] and alloying elements[38, 46, 47]. The magnetic properties of iron affects its interaction with hydrogen differently to other bcc transition metals.

The solubility of hydrogen in α -Fe, the principal component of steel, is low resulting in rapid diffusion throughout its bulk[48]. Nonetheless, hydrogen charging during tensile experiments identified increased susceptibility to hydrogen embrittlement[49]. Consequently the accumulation and trapping of hydrogen causes significant changes in the mechanical properties[5, 50]. Under hydrogen-rich conditions, α -Fe has been observed to undergo large lattice contractions[51, 52] and form hydride phases[53, 54]. In other materials such as Ni and Pd, phenomena such as superabundant vacancy formations have been detected in these hydrogen rich conditions[52, 55]. In these systems evidence from theoretical models including density functional theory (DFT) has shown hydrogen to stabilise vacancies leading to the growth of voids and bubbles. Recently developed interatomic potentials have shown how supersaturation of hydrogen gas can significantly disrupt the local atomic structure around dislocation loops[13]. Hydrogen is also known to promote plasticity by increasing the mobility of dislocations, the hydrogen-enhanced local plasticity mechanism, which can lead to localised plastic collapse and failure[56]. Precise understanding of hydrogen interactions are therefore required to predict the evolution of materials in hydrogen rich environments.

Theories investigating hydrogen embrittlement have included hydrogen-enhanced decohesion[57] and hydrogen-enhanced local plasticity[56] with recent evidence highlighting the role of vacancy-assisted embrittlement mechanisms. Surprisingly, early investigations into hydrogen-vacancy complexes in α -Fe were examined in the context of plasma facing components in fusion reactors rather than embrittlement[28]. Early implantation-annealing experiments identified vacancies to be trapped in vacancies[1, 2]. Effective-medium theory (EMT) was later used to propose monovacancies to trap multiple hydrogen atoms[58]. Whilst the mechanism is not contested, discrepancies between the number of hydrogen which can be trapped by a single vacancy are found between different models. Recent DFT calculations[11, 12], which predict up to six hydrogen may be trapped, have shown excellent agreement with desorption stages in the ion-beam implantation-annealing experiments[1, 2]. More recent calculations have shown implanted He can trap as many as eight hydrogen[59].

Commercial tokamak fusion reactors intend to use the efficient mixture of deuterium-tritium (^2H - ^3H) fuel re-

quiring tritium breeding rates from Li breeding blankets to compensate for the tritium which penetrates and permeates plasma-facing components. Further, transmutation products created through neutron capture and emission can generate hydrogen isotopes deep inside structural materials. Whilst hydrogen can induce embrittlement further considerations must be paid to tritium which is radioactive. Due to the long life of tritium, which has a half-life of 12.3 years, trapping to irradiation-induced defects need to be considered for any waste management strategy[60]. When investigating the long term effects of hydrogen adsorption, implantation and permeation most theoretical investigations rely solely on calculations of protium (^1H) as a qualitative surrogate for the heavier hydrogen isotopes. Limited investigations have been sought to quantify kinetic isotope effects of either deuterium or tritium in proposed materials for fusion powerplants. Many open questions concerning the relative behaviour of different hydrogen isotopes remain unanswered. Will the heavier isotopes have a greater propensity to be trapped? Will they replace protium in vacancies or will tritium be more strongly bound to free surfaces?

In order to address concerns as to whether different hydrogen isotopes will have different characteristic behaviours or trapping abilities in iron and steel we have carried out a systematic quantitative investigation using the density functional theory method with quantum energy corrections. Throughout the paper we shall label hydrogen without zero-point energy corrections as H. Protium, deuterium and tritium shall be labelled ^1H , ^2H and ^3H , respectively. The paper is organised as followed. The computational details of the DFT calculations are first outlined in Sec. II, followed by an explanation of the elastic correction, calculation of relaxation volume tensors and finally the vibrational analysis approach to determine zero point energy corrections for protium, deuterium and tritium. In Sec. III we provide a critical assessment of the 0 K stabilities of each hydrogen isotope in bulk (Sec. III A 1), mono-vacancies (Sec. III B 1), decorating self-interstitial atoms (SIA) (Sec. III C) and low index surfaces (Sec. III D 1). Interactions between multiple hydrogen isotopes in solution are considered in Sec. III A 3. For each environment (bulk, vacancy and surface) we also consider the interaction between hydrogen with Cr in the dilute limit (Sections III A 2, III B 2 and III D 2, respectively). Dipole tensors and relaxation volumes of hydrogen in iron are presented in Sec. III E. A summary and concluding remarks as to the stability of the hydrogen isotopes are drawn together in Sec. IV.

II. METHODOLOGY

A. Density Functional Theory

Density functional theory (DFT) calculations have been performed using the Vienna *ab initio* simulation

package (VASP) [61–64] version 5.4.1. All calculations considered collinear spin-polarisation, used projector augmented wave (PAW) pseudopotentials [65, 66] and treated exchange-correlation using the GGA functional of Perdew, Burke and Ernzerhof (PBE) [67, 68]. Plane-waves to construct the electronic basis were delimited by a cutoff energy at 500eV. A k-point mesh was constructed using the Monkhorst-Pack method[69] ensuring a minimum linear density between k-points of 0.015\AA^{-1} . For a 250 atom cell constructed from $5 \times 5 \times 5$ bcc unit cells this equates to a $3 \times 3 \times 3$ Γ -centred grid. Brillouin zone integration was performed using the Methfessel-Paxton method[70] with a smearing of 0.1 eV. Convergence of the electronic states during self-consistent field optimisation was set to tolerances below 10^{-6} eV. Calculations fixed unit cell volume and shape, allowing atomic positions to relax until the Hellmann-Feynman forces on each atom were below $5 \text{ meV}/\text{\AA}$ using the quasi-Newton RMM-DIIS algorithm[71]. All calculations implemented 3D periodic boundary conditions. With the exception of surface calculations, unless stated otherwise, simulation cells are constructed from $5 \times 5 \times 5$ bcc unit cells (250 atom).

B. The Dipole Tensor, Elastic Correction and Relaxation Volume

The macroscopic stress of a simulation box equals the average internal stress:

$$\bar{\sigma}_{ij} = \frac{1}{V_{\text{cell}}} \int \sigma_{ij} dV \quad (1)$$

where V_{cell} is the cell volume. The dipole tensor P_{ij} of a localised defect, such as a hydrogen interstitial or vacancy-hydride complex, can be evaluated from the stress developed in the simulation box [72, 73]:

$$P_{ij} = V_{\text{cell}}(C_{ijkl}\epsilon_{kl}^{\text{app}} - \bar{\sigma}_{ij}). \quad (2)$$

Since the dimensions of simulation cells are fixed, there is no applied stress $\epsilon_{kl}^{\text{app}} = 0$. An elastic correction energy accounting for the elastic interaction between images in periodic boundary conditions can be calculated using the dipole tensor of the defect and the anisotropic elastic Green's function $G_{ij}(\mathbf{r})$ [42, 73]:

$$E_{\text{el}}^{\text{corr}} = E_{DD} + E_{\text{strain}}^{\text{corr}} \quad (3)$$

where E_{DD} is a dipole-dipole representation of the elastic interaction between a defect and its periodic images and $E_{\text{strain}}^{\text{corr}}$ is the self-strain correction energy.

The dipole interactions are the sum of elastic interactions with its image at $\mathbf{R}_{\mathbf{n}}$, which is conditionally convergent[74], and a regularisation term to ensure con-

vergence:

$$E_{DD} = \frac{1}{2} \sum_{\mathbf{n} \neq 0} P_{ij} P_{kl} \frac{\partial}{\partial x_j} \frac{\partial}{\partial x_l} G_{ik}(\mathbf{R}_{\mathbf{n}}) - \frac{1}{2V_{\text{cell}}} \sum_{\mathbf{n} \neq 0} \int_{V_{\text{cell}}} P_{ij} P_{kl} \frac{\partial}{\partial x_j} \frac{\partial}{\partial x_l} G_{ik}(\mathbf{R}_{\mathbf{n}} - \mathbf{r}) d^3r \quad (4)$$

The self-strain correction term corrects the linear elastic part of the strain field using the far-field approximation:

$$E_{\text{strain}}^{\text{corr}} = -\frac{1}{V_{\text{cell}}} \int_{V_{\text{cell}}} P_{ij} P_{kl} \frac{\partial}{\partial x_j} \frac{\partial}{\partial x_l} G_{ik}(\mathbf{r}) d^3r \quad (5)$$

We calculated the energy correction using the CALANIE code [74] wherein the elastic Greens function and its derivatives are calculated numerically using the Barnett approach[75].

The relaxation volume tensor Ω_{ij} characterises the change of the shape and volume of a sample after inserting a defect. It is related to the dipole tensor through the elastic compliance tensor S_{ijkl} :

$$\Omega_{ij} = S_{ijkl} P_{kl}, \quad (6)$$

where $\mathbf{S} = \mathbf{C}^{-1}$, satisfying the condition $C_{ijkl} S_{klmn} = \frac{1}{2}(\delta_{im}\delta_{jn} + \delta_{in}\delta_{jm})$. The relaxation volume can be computed as the trace of the relaxation volume tensor:

$$\Omega^{\text{rel}} = \text{Tr}(\Omega_{ij}). \quad (7)$$

As a simple illustration, the relaxation volume of a vacancy is negative, whereas for a self-interstitial atom, it is positive [3, 42, 76]. The relaxation volume has proven to be a remarkably universal concept in the study and characterisation of defects [3, 42, 72, 76–82]. Relaxation volumes in this work are calculated through post-processing the dipole tensor of the DFT calculation using the CALANIE code[74].

C. Zero Point Energies and the Classical Mass Approximation

The zero point motion of hydrogen is non-negligible requiring a zero-point energy (ZPE) correction to be applied by summing the zero-point vibrational energies of hydrogens normal modes:

$$E_{\text{ZPE}} = \sum_m \frac{1}{2} h\nu_m \quad (8)$$

where h is Plank's constant and ν are the real normal mode frequencies.

Within the harmonic approximation, the dynamic modes of a collection of particles with mass M and at

positions \mathbf{r} in real-space, may be obtained as the eigenfrequencies of the Dynamical matrix $D_{ij}^{\alpha\beta}$:

$$D_{ij}^{\alpha\beta} = \frac{1}{\sqrt{M^\alpha M^\beta}} \Phi_{ij}^{\alpha\beta} e^{-i\mathbf{q}\cdot\mathbf{r}} \quad (9)$$

$$= \frac{1}{\sqrt{M^\alpha M^\beta}} C_{ij}^{\alpha\beta} \quad (10)$$

which is the mass-reduced Fourier transform of the force-constants matrix, whose elements contains the second derivatives of the potential energy surface with respect to changes in positions:

$$\Phi_{ij}^{\alpha\beta} = \frac{\partial^2 V}{\partial x_i^\alpha \partial x_j^\beta} \quad (11)$$

i, j span the particles whilst α, β span the Cartesian directions x, y, z and V relates to the Born-Oppenheimer energy surface. Within the Kohn-Sham framework of DFT, the Born-Oppenheimer energy surface is independent of the masses of nuclei. The ensemble of atoms produce the *external field* which is taken as a Coulomb interaction ($-\sum_\alpha Z^\alpha/|\mathbf{r}^i - \mathbf{R}^\alpha|$) mediated by the atomic charges Z . As protium (^1H), deuterium (^2H) and tritium (^3H) each only possess a single proton (the isotopes differ in the neutrons bound to the nucleus), the electronic structure of each isotope will be equivalent within the framework of our calculations. It is important to note that harmonic lattice dynamics in this form are derived from a Taylor expansion where equilibrium is assumed, i.e. Hellmann-Feynman forces are zero. The solutions are therefore only valid at stationary states where the equilibrium condition is satisfied. Quasi-harmonic effects are not considered in this work.

The eigenfrequencies ω (and eigenvectors ϵ) are derived by diagonalising the Dynamical matrix $D_{ij}^{\alpha\beta}$:

$$(D_{ij}^{\alpha\beta} - \omega_{m,\mathbf{q}}^2) \epsilon_{m\alpha,i\mathbf{q}} = 0 \quad (12)$$

Alternatively we may recast the eigenequation in terms of the Fourier transform of the force constants matrix $C_{ij}^{\alpha\beta}$ which emphasises the eigensolutions are dependent of the mass of each atom. In this work we will only consider modes at $\Gamma(\mathbf{q} = \mathbf{0})$ so we drop the index for brevity. The eigenfrequencies ω are related to the mode frequencies as $\nu_m = \omega_m/2\pi$.

$$D_{ij}^{\alpha\beta} \epsilon_{m\alpha,i} = \omega_m^2 \epsilon_{m\alpha,i} \quad (13)$$

$$\frac{1}{\sqrt{M^\alpha M^\beta}} C_{ij}^{\alpha\beta} \epsilon_{m\alpha,i} = \omega_m^2 \epsilon_{m\alpha,i} \quad (14)$$

$$C_{ij}^{\alpha\beta} \epsilon_{m\alpha,i} = \omega_m'^2 \epsilon_{m\alpha,i} \quad (15)$$

We subsume the mass dependence into the eigenfrequency $\omega' = \omega\sqrt{M^\alpha M^\beta}$ which is then solved using the secular equation[83]:

$$\det \left| C_{ij}^{\alpha\beta} \epsilon_{m\alpha,i} - \omega_m'^2 \epsilon_{m\alpha,i} \right| = 0 \quad (16)$$

Due to the mass dependence, the ZPE correction will be different for each of hydrogens isotopes. As a consequence, the uncorrected DFT energies will be the same for each isotope but the ZPE corrected energies will necessarily differ. That isotropic substitution is only reflected in the mass in the dynamic matrix has provided a route to interpret Raman experiments from frequency shifts of substituted elements[84, 85].

Noting the mass of iron is substantially greater than hydrogen, then we may make the reasonable approximation that lattice vibrations can be decoupled from the localised hydrogen vibrational modes[86, 87]. This is the mass approximation. Neglecting contributions from iron to the ZPE correction within the Einstein approximation is often applied when studying the Fe-H binary system [11, 59, 88, 89]. In practise, this is achieved by fixing the positions of the iron atoms (effectively treating their mass as infinite) and calculating the Hessian with displacements of hydrogen atoms. We use a displacement of 0.015\AA when calculating the force constants via the finite difference method. The characteristic equation is now only dependent upon the mass of hydrogen. Since $C_{ij}^{\alpha\beta}$ will be the same regardless of which hydrogen isotope is present in the system, we can relate the eigenfrequencies of deuterium and tritium (ω') in proportion to the eigensolutions for protium (ω). If we assign the notion $\omega(^n\text{H})$ as the eigenfrequency for the system whose hydrogen isotopes are all ^nH , then:

$$\omega_m^2(^n\text{H}) = \frac{1}{\sqrt{M^{n\text{H}} M^{n\text{H}}}} \omega_m^2(^1\text{H}) \quad (17)$$

That is, within the DFT framework using both harmonic and mass approximations, swapping all protium for either deuterium or tritium allows us to calculate the ZPE correction as a simple scaling relative to the ZPE correction of protium:

$$\omega_m(^2\text{H}) = \frac{\omega_m(^1\text{H})}{\sqrt{2}} \implies E_{\text{ZPE}}(^2\text{H}) = \frac{E_{\text{ZPE}}(^1\text{H})}{\sqrt{2}} \quad (18)$$

$$\omega_m(^3\text{H}) = \frac{\omega_m(^1\text{H})}{\sqrt{3}} \implies E_{\text{ZPE}}(^3\text{H}) = \frac{E_{\text{ZPE}}(^1\text{H})}{\sqrt{3}} \quad (19)$$

We note that the ZPE correction using the harmonic approximation neglects anharmonic effects as well as other quantum mechanical effects such as tunnelling such that the correction is incomplete[90, 91]. Nonetheless, DFT comparisons between harmonic and anharmonic calculations of interstitial hydrogen in Al has shown only small differences[92]. Further, our calculations of the ZPE of molecular hydrogen and deuterium (Table I) closely match experiment such that we may take the harmonic approximation to be sufficient in our work. On the other hand, when studying thermodynamics of hydrogen in $\alpha\text{-Fe}$ the quantum fluctuations and hydrogen hopping become significant and must be fully considered[93, 94].

TABLE I. Zero point energy of molecular hydrogen ($^1\text{H}_2$), molecular deuterium ($^2\text{H}_2$) and molecular tritium ($^3\text{H}_2$), presented in eV.

Dimer	DFT				Experiment
	Present	Ref.96	Ref.97	Ref.12	
$^1\text{H}_2$	0.275	0.288	0.27	0.28	0.272 ^a , 0.258 ^b
$^2\text{H}_2$	0.196	0.202	0.19		0.19 ^b , 0.1917 ^c
$^3\text{H}_2$	0.160	0.170			

^a Ref. 95

^b Ref. 98

^c Ref. 99

We optimised the bond length of a dimer in vacuo within a $14 \times 14 \times 14 \text{ \AA}^3$ box before the vibrational analysis was performed. The relaxed bond length was calculated to be 0.750 \AA in good agreement with previous calculations[12, 22, 61] and the experimental value of 0.741 \AA [95]. The ZPE's calculated in Table I did not use the mass approximation but the $1/\sqrt{2}$ and $1/\sqrt{3}$ scaling for deuterium and tritium is evident.

III. RESULTS

A. Bulk

1. Hydrogen isotopes in solution and their diffusion in pure iron

The body centered cubic (bcc) lattice offers two high symmetry interstitial sites, tetrahedral and octahedral, that a hydrogen isotope may occupy. The preference for hydrogen to reside in the tetrahedral site is well documented in ab initio studies with experimental evidence noting hydrogen will occupy the tetrahedral site a low temperatures. Hydrogen atoms moving to occupy the octahedral site becomes feasible at high temperatures as is common to many bcc metals[100–104]. Our results agree with previous studies showing hydrogen to reside in the tetrahedral site which is 0.133 eV more favorable than the octahedral site.

The heat of solution (E_{sol}) is defined as the energy released when a hydrogen atom takes an interstitial site relative to molecular hydrogen:

$$E_{sol}^{site} = E(H_{site}) - E_0 - \frac{1}{2}E(H_2) \quad (20)$$

$E(H_{site})$ is the energy of the bcc iron lattice containing an interstitial hydrogen isotope in either site=tetrahedral or site=octahedral. E_0 is the energy of the perfect bcc iron lattice containing no defects the same size and volume and $E(H_2)$ is the energy of an isolated hydrogen molecule. For contributing terms which contain hydrogen, the zero point energies for a hydrogen isotope are added to each term. All terms include an elastic correction.

TABLE II. Energy of solution (Eqn. 20) for hydrogen isotopes in tetrahedral and octahedral interstitial positions within bcc iron. The diffusion barrier ΔE_{sol} for a TET \rightarrow OCT \rightarrow TET transition and the rotational TET \rightarrow TET ($\Delta E'_{sol}$) is provided for each isotope. Energies are presented in eV. Zero-point energies of protium, ZPE(^1H), are presented in eV/H. Energies of solution for the unrelaxed configurations are presented in the final column. An energy difference $\Delta E_{sol}=0.47$ eV is given in Ref. 11 (without ZPE correction). Experimental activation barriers range between 0.035 eV to 0.142 eV[105].

	DFT			Exp. Ref.4	DFT(Unrel.) Present
	Present	Ref.12	Ref.11		
E_{sol}^{TET}:					
H	0.207	0.13	0.20		0.459
ZPE (^1H)	0.238	0.24	0.234		0.285
^1H	0.306	0.23	0.301	0.296	0.606
^2H	0.276				0.563
^3H	0.263				0.544
E_{sol}^{OCT}:					
H	0.341	0.27	0.33		0.933
ZPE (^1H)	0.133	0.12			0.200
^1H	0.331	0.26			0.996
^2H	0.333				0.978
^3H	0.333				0.969
$\Delta E_{sol} = E_{sol}^{OCT} - E_{sol}^{TET}$:					
H	0.133	0.148	0.13		0.474
^1H	0.026	0.035			0.389
^2H	0.056				0.414
^3H	0.070				0.425
$\Delta E'_{sol}$: T \rightarrow T transition					
H	0.089	0.090	0.088		
ZPE(^1H) ^a	0.189	0.190	0.188 ^b		
^1H	0.042	0.044	0.042		
^2H	0.056				
^3H	0.063				

^a Zero-point energy at the transition state

^b Adding ZPE at the tetrahedral interstitial (0.234 eV) to the reported difference ΔZPE (-0.046 eV).

The heat of solution for hydrogen (without zero point energy correction) as well as hydrogen isotopes in both interstitial sites are provided in Table II. Where results are available for hydrogen and protium we find good agreement with previous theoretical studies for both heats of solution and the ZPE[11, 12]. The energy of solution for protium (0.306 eV) is in excellent agreement with experimental results (0.296 eV [4]). The vibrational analysis, from which the zero point energies are calculated, indicate that the octahedral site at 0K is a second order transition state for all hydrogen isotopes. Each have near degenerate heats of solution. Due to additional degrees of freedom the zero point energies in the tetrahedral site are larger than at the octahedral site resulting in a reduction in the ZPE corrected diffusion barrier for a tetrahedral

→ octahedral → tetrahedral transition. Generally transition states only have a single negative eigenvalue[106]. However, since the octahedral site has high symmetry and connects multiple potential wells (leading to tetrahedral sites), from which each site is equally accessible [107], it is a valid transition state with degenerate negative eigenvalues [12].

A previous investigation has shown that without ZPE corrections, a tetrahedral → tetrahedral transition has a migration barrier of 0.09 eV[12] which is less than the tetrahedral → octahedral → tetrahedral path (T→O→T). However, when quantum fluctuations are accounted for (excluding tunneling) the barriers become 0.044eV and 0.035 eV, respectively [12]. That is to conclude both barriers are nearly equivalent and small. We use the Climbing Image Nudge Elastic Band method to find the minimum energy path for the T→T transition and find an activation barrier of 0.089 eV. Application of the ZPE correction reduces the barrier for protium to be 0.042 eV exactly matching the results of Jiang and Carter[11]. As such, our results also show the T→O→T transition to be favorable for protium. Experimental investigations provide a rather a range of activation energies between 0.035-0.142 eV[105]. Rather surprisingly the barrier for both transitions is degenerate for deuterium whilst the rotational path has the lowest barrier for tritium (Table II). We visualise the energy barriers in Figure 1a.

Within this work we are using the assumption that due to the mass difference between iron and hydrogen, lattice vibrations may be decoupled from the localised hydrogen vibrational modes[86, 87]. If a further approximation is made taking the lattice vibrations and the minimum and saddle points in a transition, then Kehr[87] simplified the relations used in Ref. 86. Where the limit $h\nu_H \gg k_B T$ is valid, then the diffusion coefficient may be approximated from the following Arrhenius relation:

$$D = \frac{n}{6} a^2 \frac{k_B T}{h} \exp\left(-\frac{\Delta E}{k_B T}\right) \quad (21)$$

where n is the number of equivalent jump paths ($n = 2$ for the T→O→T transition, $n = 4$ for the T→T transition), a is the jump length, T is the temperature and ΔE is the ZPE corrected migration barrier. As noted in Ref. 11, at room temperature $k_B T \approx 0.025$ eV which is an order of magnitude smaller than the the ZPE corrections ($h\nu_H$) at either the tetrahedral (0.238 eV/¹H, 0.168 eV/²H, 0.138 eV/³H) or octahedral (0.133 eV/¹H, 0.094 eV/²H, 0.077 eV/³H) sites. We have used activation barriers for the T→O→T transition for protium and the T→T transition for tritium. Since both pathways are degenerate for deuterium we take $n = 4 + 2$. It is important to note that at low temperatures the dominant mechanism for hydrogen diffusion will be quantum diffusion[108] which has not been considered here.

Considering the approximations made, the temperature dependent diffusion coefficient agrees reasonably

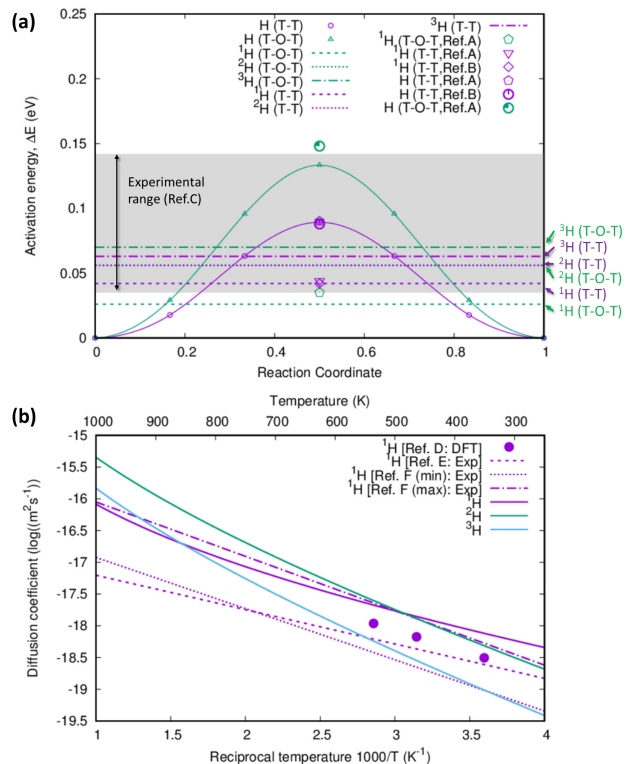


FIG. 1. Migration of hydrogen isotopes in pristine α -Fe. (a) Activation (migration) energy barriers of each isotope before and after ZPE correction. Migration via the octahedral rank 2 saddle point (T-O-T) is green. Direct rotational transition to adjacent tetrahedral site (T-T) is purple. Uncorrected barriers have solid lines. Dash types differentiate protium (dash), deuterium (fine dash) and tritium (dot-dash). Results from previous DFT calculations (Ref.A=[12] and Ref.B=[11]) and experimental ranges (Ref.C=[105]) as shown for comparison. (b) Diffusion coefficients (Eqn. 21) of hydrogen isotopes (protium ¹H [purple], deuterium ²H [green] and tritium ³H [blue]). Density functional theory results for the T→O→T transition from Ref. 12 (Ref.D). Experimental diffusion coefficients from Ref. [109] (Ref.E) and Ref. [110] (Ref.F, taking the minimum and maximum values of D_0 and ΔE).

well with previous DFT[12] and experimental curves[109, 110] for protium diffusion in pure iron (Figure 1(b)). As could be inferred for the larger migration barriers, the heavier isotopes of hydrogen have lower diffusivity at low temperatures which is consistent with previous studies in bcc metals[22, 96, 111]. Nonetheless, all hydrogen isotopes remain highly mobile compared to small impurities such as carbon or nitrogen whose diffusion coefficient is of the order 10^{-12} m²s⁻¹ at room temperature[48]. Remarkably, the under the current approximations deuterium is predicted to become more mobile than protium at the operating temperatures of D-T fusion tokamaks (600-800 K). This is due to the degenerate barrier for both transitions increasing the probability of a successful transition for a given attempt frequency. Whilst these results are interesting we must caution anharmonic effects have

not treated in the analysis which has been shown to cause deviation from Arrhenius behaviour[93, 94].

It should be additionally noted that the $T \rightarrow O \rightarrow T$ energy barrier is significantly greater when hydrogen is placed in tetrahedral and octahedral positions and iron atoms are fixed in their ideal lattice sites (unrelaxed, Table II). This elucidates how susceptible the activation energy will be to thermally driven distortions about their lattice sites. As such, we must consider the activation energies in DFT calculations to represent a lower threshold.

To verify hydrogen modes are decoupled from iron we calculate the phonon dispersion for each isotope in the tetrahedral and octahedral sites (Figure 2). We also provide the phonon dispersion at the tetrahedral-tetrahedral transitional state. To calculate the full Hessian we used density functional perturbation theory[83]. Due to computational constraints of this method we used a smaller simulation cell constructed from $3 \times 3 \times 3$ bcc unit cells (54 Fe, 1 H). Since we consider the vibrational modes of iron we do not apply the mass approximation and explicitly include the mass of each isotope in the mass reduced force constants. The results show the decoupling is a good approximation as (1) hydrogen bands are extremely flat across all considered wave-vectors and (2) the phonons for iron are almost identical whether the system contains protium, deuterium or tritium. Negative eigenfrequencies reflect the negative curvature of the potential energy surface at the octahedral site. We may also use these calculations to provide an estimate of the error in the mass approximation. The highest bands for protium, deuterium and tritium in the tetrahedral positions have frequencies 43.82 THz, 31.19 THz and 25.64 THz, respectively. Using the mass approximation (Eqns. 18-19) from the frequency of protium we would estimate the deuterium band to shift to $43.82/\sqrt{2} = 30.87$ THz and the tritium band to become $43.82/\sqrt{3} = 25.20$ THz. As such we take the error of the approximation to be within 2%.

2. Hydrogen isotopes in solution near Cr solutes

Radiation resistant ferritic steels typically have approximately 9% Cr content[16, 112]. At this concentration, the enthalpy of mixing is negative indicating the propensity to form a mixed solid solution[46, 113–120]. Above approximately 12%, the enthalpy of solution becomes positive due to magnetic frustration between the iron and chromium atoms results in a region of spinodal decomposition and the segregation of chromium into precipitates[115, 121, 122]. Since the steels of interest have a *low* Cr concentration where the solutes have a propensity to be maximally separated to avoid non-collinear magnetic frustration[38, 47], we only consider hydrogen interactions with Cr in the dilute limit. The binding interaction between the Cr and H isotopes are presented in Table III for multiple octahedral and tetrahedral sites. All octahedral sites are rank 2 saddle points and the tetrahedral sites are minima in the Born-

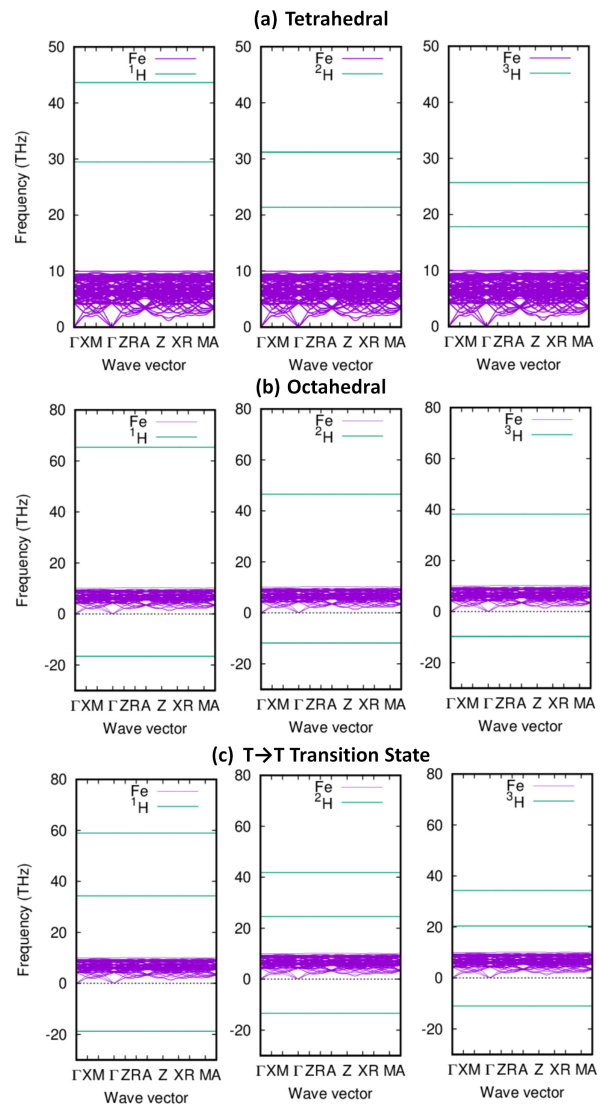


FIG. 2. Phonon dispersion of hydrogen isotopes in (a) tetrahedral and (b) octahedral interstitial sites as well as the (c) $T \rightarrow T$ saddle point, within α -Fe calculated using a $3 \times 3 \times 3$ bcc unit cell (54 iron on lattice, 1 hydrogen interstitial). Phonons of iron and hydrogen are differentiated by purple and green curves, respectively. Wave-vectors are defined according to tetragonal symmetry with $\Gamma=[0,0,0]$, $X=[0, \frac{1}{2}, 0]$, $M=[\frac{1}{2}, \frac{1}{2}, 0]$, $Z=[0,0, \frac{1}{2}]$, $R=[0, \frac{1}{2}, \frac{1}{2}]$, $A=[\frac{1}{2}, \frac{1}{2}, \frac{1}{2}]$. The point symmetry for hydrogen in the transitional states are different but we retain the same wave-vector path and nomenclature. The highest band for the tetrahedral site and the soft band in the octahedral site have degeneracy.

Oppenheimer energy surface.

In general, the systems relax to increase the distance between the two species. This is also reflected in the binding energies which show that the interactions are repulsive (see Figure 3). For hydrogen in the tetrahedral site, the attraction only becomes weakly attractive for separations greater than $2a$. This is in contrast to other solute substitutions where synergistic effects have

been observed to increase the trapping ability[59]. The low charge density of a He_{Fe} enables 8 hydrogen to be exothermically trapped. We note the relaxation volume of this substitute is 1.00\AA^3 giving it an effective volume ($\Omega_{\text{sol}}^{\text{Fe}} = \Omega^{\text{rel}} + \Omega_0^{\text{Fe}} = 12.34\text{\AA}^3$) which is 8% larger than the iron host elements. In combination with the low charge density this reduced the dissolution energy for He near the complex. Conversely, the relaxation volume of Cr is 2.56\AA^3 ($\Omega_{\text{sol}}^{\text{Fe}} = 13.9\text{\AA}^3$) such that it elastically 20% larger. That the complex is significantly oversized despite the similar ideal lattice parameters of Fe and Cr can be attributed to a magnetovolume effect** from the enhancement of the magnetic moment of the Cr atom ($-1.85\mu_B$ relative to $\pm 1.08\mu_B$ in bulk). The negative sign indicates the moment opposes that of the iron atoms.

We may also calculate the energy of mixing using:

$$\Delta E_{\text{mix}} = \frac{E(\text{CrH}) - n_{\text{Fe}}E(\text{Fe}) - n_{\text{Cr}}E(\text{Cr}) - \frac{n_{\text{H}}}{2}E(\text{H}_2)}{n_{\text{Fe}} + n_{\text{Cr}} + n_{\text{H}}} \quad (22)$$

In the absence of hydrogen, the energy of mixing (which for FeCr is equivalent to the energy of mixing as both share a bcc groundstate) is -0.59 meV at the concentration 0.4%. When hydrogen is present the mixing energy is positive in all cases (Table IV) indicating the Cr and H want to segregate. This is consistent with the repulsive binding energies when the interatomic separation is less than $2a$.

A small spontaneous formation of a magnetic moment in hydrogen is noted in both tetrahedral and octahedral interstitial sites in pure iron with a value of $-0.02\mu_B$ in both cases (Table IV). With the exception of the nearest neighbouring tetrahedral and octahedral sites to Cr_{Fe} , the same moment is formed. In these nearest neighbour positions its moment is reduced to $-0.01\mu_B$ and corresponds to where the binding energy is most repulsive and the energy of mixing is greatest. The magnetic moment of Cr is found to be reduced relative to its isolation in the iron bulk as hydrogen approaches.

In pure iron, the $T \rightarrow O \rightarrow T$ path was shown to have a small barrier once adjusted for zero point energies and become comparable to the barrier of the $T \rightarrow T$ transition [12]. A full determination of the transition mechanism would require application of techniques such as the nudge elastic band method and will be considered in future work. However, it is important to note that for protium, deuterium and tritium, the asymmetric energy barriers between the tetrahedral and octahedral sites due to the presence of the Cr solute range between 21-40 meV, 52-71 meV and 68-84 meV, respectively. A recent cluster expansion model was used to show that for low homogenous Cr concentrations protium diffusivity decreases[14]. Our calculations indicate the same will be true for all hydrogen isotopes. However, despite the barrier ranges having a similar range (≈ 20 meV), the reduction in diffusivity will likely be less pronounced for deuterium and tritium due to their larger barriers and the exponential decay term of the Arrhenius law.

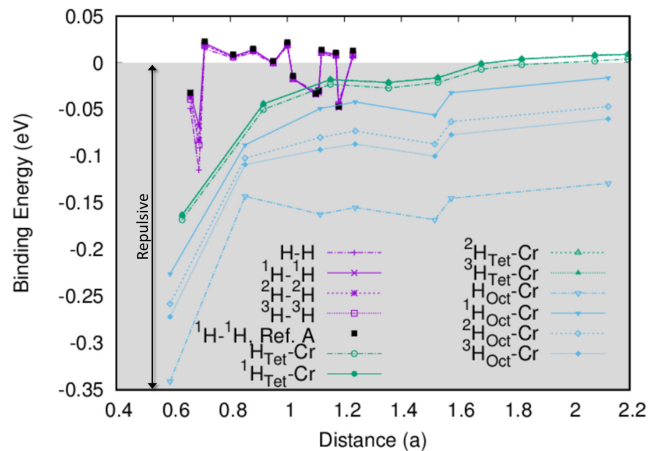


FIG. 3. ${}^n\text{H}$ - ${}^n\text{H}$ (purple), ${}^n\text{H}$ -Cr binding energies in α -Fe. Hydrogen in tetrahedral and octahedral interstitial sites are shown in green and blue, respectively. Dash types reflect the hydrogen isotope ($n=1,2,3$). Attractive interactions have a positive binding energy. Distances are provided in lattice parameter units ($a=2.832\text{\AA}$). DFT calculations for protium (${}^1\text{H}$ - ${}^1\text{H}$) from Ref. 88 (labelled Ref.A) extracted from Ref. 123 are shown for comparison.

3. H-H, D-D and T-T Interactions in pure iron

Understanding of hydrogen-hydrogen interactions when in solution are critical to predict phenomena such as the clustering of hydrogen and formation of H-bubbles in metals[124, 125]. To quantify the interaction between a pair of hydrogen isotopes we may use the binding energy E_B^{HH} :

$$E_B^{\text{HH}} = 2E(\text{H}_{\text{TET}}) - E(2\text{H}_{\text{TET}}) - E_0 \quad (23)$$

where $E(\text{H}_{\text{TET}})$ is the energy of a single hydrogen isotope in a tetrahedral lattice site within a bcc iron lattice. $E(2\text{H}_{\text{TET}})$ is the energy of the system containing two hydrogen isotopes in solution, and E_0 is the energy of the perfect bcc iron lattice containing the same number of iron atoms as the other two cases (250 in our calculations). Within this definition a positive binding energy is attractive.

Binding energies for pairs of each isotope are presented in Table V and Figure 3, with comparative data for protium[88, 89]. The DFT parameters in Ref. 88 are nearly identical, including the use of an elastic correction, albeit they use 450 eV cut off energy accounting for the small discrepancies. For tetrahedral sites which are 1st nearest neighbour the configuration is unstable leading to the migration of one of the hydrogen to increase the interatomic separation. At the second nearest and third nearest neighbouring distances, the hydrogen interactions are repulsive. Beyond the third nearest neighbouring sites all hydrogen isotope interactions are attractive until separated by over a lattice parameter when they become repulsive. This indicates a propensity for clustering. Recent calculations reveal that the forma-

TABLE III. Relaxed interatomic distances (in lattice parameter units, $a = 2.832\text{\AA}$), binding energies (eV) and energy of mixing (meV) between a solute Cr_{Fe} substitution and interstitial hydrogen isotopes in α -Fe. Hydrogen is considered with initial positions in octahedral and tetrahedral interstitial sites. Tetrahedral sites are labelled relative to their neighbouring octahedral site ($|\Delta x| = |\Delta y| = \frac{1}{4}a$).

	Cr-H distance		Binding Energy					$\Delta E = E_{\text{Oct}} - E_{\text{Tet}}$			
	Initial	Relaxed	H	ZPE	^1H	^2H	^3H	H	^1H	^2H	^3H
Octahedral											
A	$\frac{1}{2}a=0.707a$	0.852a	-0.143	0.190	-0.088	-0.102	-0.109				
B	$\frac{1}{2}a=0.5a$	0.589a	-0.341	0.130	-0.266	-0.258	-0.272				
C	$\frac{\sqrt{5}}{2}a=1.118a$	1.115a	-0.162	0.133	-0.049	-0.080	-0.093				
D	$\sqrt{\frac{3}{2}}a=1.225a$	1.238a	-0.155	0.132	-0.043	-0.073	-0.087				
E	$\frac{3}{2}a=1.5a$	1.517a	-0.168	0.134	-0.056	-0.087	-0.010				
F	$\sqrt{\frac{5}{2}}a=1.581a$	1.576a	-0.145	0.133	-0.032	-0.063	-0.077				
G	$\frac{3}{\sqrt{2}}a=2.121a$	2.215a	-0.129	0.133	-0.016	-0.047	-0.060				
Tetrahedral											
A- Δx	$\frac{\sqrt{5}}{4}a=0.559a$	0.631a	-0.168	0.238	-0.163	-0.163	-0.163	-0.026	-0.063	-0.060	-0.054
A+ Δx	$\frac{\sqrt{13}}{4}a=0.901a$	0.916a	-0.050	0.237	-0.044	-0.044	-0.044	0.092	0.045	0.058	0.065
A- Δy	\rightarrow Equiv. to A- Δx										
A+ Δy	\rightarrow Equiv. to A+ Δx										
B $\pm\Delta x$	\rightarrow Equiv. to A+ Δx										
B $\pm\Delta y$	\rightarrow Equiv. to A+ Δx										
C- Δx	$\frac{\sqrt{21}}{4}a=1.145a$	1.151a	-0.023	0.239	-0.018	-0.018	-0.018	0.130	0.023	0.054	0.068
C+ Δx	$\frac{\sqrt{29}}{4}a=1.347a$	1.355a	-0.027	0.238	-0.021	-0.021	-0.021	0.126	0.021	0.052	0.079
C- Δy	\rightarrow Equiv. to C- Δx										
C+ Δy	\rightarrow Equiv. to C+ Δx										
D $\pm\Delta x$	$\frac{\sqrt{37}}{4}a=1.521a$	1.528a	-0.021	0.239	-0.016	-0.016	-0.016	0.145	0.040	0.071	0.084
D $\pm\Delta y$	\rightarrow Equiv. to D $\pm\Delta x$										
E- Δx	$\frac{\sqrt{53}}{4}a=1.820a$	2.078a	0.002	0.238	0.008	0.008	0.008	0.129	0.024	0.055	0.068
E+ Δx	$\frac{\sqrt{77}}{4}a=2.194a$	2.195a	0.004	0.238	0.009	0.009	0.009	0.131	0.025	0.056	0.070
E $\pm\Delta y$	\rightarrow Equiv. to E $\pm\Delta x$										
E $\pm\Delta x$	\rightarrow Equiv. to C+ Δx										
E- Δy	\rightarrow Equiv. to A- Δy										
E+ Δy	\rightarrow Equiv. to C- Δy										
F- Δx	$\frac{\sqrt{454}}{a}=1.677a$	1.680a	-0.007	0.238	-0.001	-0.001	-0.001	0.136	0.031	0.062	0.075
F+ Δx	\rightarrow Equiv. to D+ Δx										
F- Δy	\rightarrow Equiv. to C- Δy										
F+ Δy		1.822a	-0.002	0.238	0.004	0.004	0.004	0.141	0.036	0.067	0.080

tion energy for some FeH hydrides are of the order 0.01 eV/H which precipitates that hydride formations may be more favorable than a random distribution in an iron matrix[125, 126]. Indeed, DFT calculations have predicted that planar hydride formations may precipitate in bcc iron[125]. However, to date, hydride inclusions have only been experimentally observed under high hydrogen pressures[53, 54, 127, 128].

Similar trends are observed for interactions between each of hydrogen's isotopes. The heavier isotopes feel greater repulsion at short distances and weaker attraction than protium in the attractive region. In combination with the lower diffusivity, this suggests protium will have a higher propensity to clustering than deuterium or tritium.

B. Vacancies

1. Trapping of hydrogen isotopes in vacancies

Vacancies have been shown to act as strong trapping sites which prevent hydrogen diffusing through bulk bcc crystals. Different minimum energy hydrogen configurations have been predicted for different bcc metals [1, 58, 129]. Unlike in the iron bulk where a hydrogen isotope in solution occupies a tetrahedral site, when in a monovacancy a *near octahedral site* (NOS) is preferential[28, 130]. Previous DFT studies have shown this results in stronger hybridisation between hydrogen's *s* electron with the *d* electrons in the neighbouring iron atoms[12]. Such an effect is also observed in Mo[131].

TABLE IV. Magnetic moments (μ_B) and energy of mixing (meV/atom) for a solute Cr_{Fe} substitution and interstitial hydrogen isotopes in α -Fe. Hydrogen is considered with initial positions in octahedral and tetrahedral interstitial sites. Tetrahedral sites are labelled relative to their neighbouring octahedral site ($|\Delta x| = |\Delta y| = \frac{1}{4}a$).

	Magnetic Moments (μ_B)		Energy of Mixing (meV/atom)			
	Cr	H	H	^1H	^2H	^3H
Octahedral						
A	-1.915	-0.022	0.774	0.981	0.921	0.894
B	-1.475	-0.011	1.562	1.530	1.540	1.544
C	-1.788	-0.021	0.818	0.796	0.803	0.806
D	-1.831	-0.021	0.869	0.854	0.859	0.861
E	-1.843	-0.022	0.713	0.693	0.699	0.702
F	-1.865	-0.022	0.844	0.824	0.830	0.832
G	-0.156	-0.021	0.777	0.758	0.763	0.766
Tetrahedral						
A $-\Delta x$	-1.718	-0.013	0.879	1.278	1.162	1.110
A $+\Delta x$	-1.887	-0.024	0.409	0.804	0.688	0.637
A $-\Delta y \rightarrow$ Equiv. to A $-\Delta x$						
A $+\Delta y \rightarrow$ Equiv. to A $+\Delta x$						
B $\pm\Delta x \rightarrow$ Equiv. to A $+\Delta x$						
B $\pm\Delta y \rightarrow$ Equiv. to A $+\Delta x$						
C $-\Delta x$	-1.846	-0.023	0.302	0.704	0.586	0.534
C $+\Delta x$	-1.808	-0.023	0.315	0.713	0.597	0.545
C $-\Delta y \rightarrow$ Equiv. to C $-\Delta x$						
C $+\Delta y \rightarrow$ Equiv. to C $+\Delta x$						
D $\pm\Delta x$	-1.847	-0.023	0.291	0.695	0.577	0.525
D $\pm\Delta y \rightarrow$ Equiv. to D $\pm\Delta x$						
E $-\Delta x$	-1.841	-0.021	0.198	0.598	0.481	0.429
E $+\Delta x$	-1.849	-0.023	0.193	0.593	0.476	0.424
E $\pm\Delta y \rightarrow$ Equiv. to E $\pm\Delta x$						
E $\pm\Delta x \rightarrow$ Equiv. to C $+\Delta x$						
E $-\Delta y \rightarrow$ Equiv. to A $-\Delta y$						
E $+\Delta y \rightarrow$ Equiv. to C $-\Delta y$						
F $-\Delta x$	-1.850	-0.023	0.235	0.636	0.518	0.466
F $+\Delta x \rightarrow$ Equiv. to D $+\Delta x$						
F $-\Delta y \rightarrow$ Equiv. to C $-\Delta y$						
F $+\Delta y$	1.853	-0.023	0.215	0.615	0.498	0.446

When a vacancy traps additional hydrogen isotopes, there are symmetrically inequivalent sites upon which the new hydrogen atom may be trapped. The preferential sites for multiple protium[12, 28] have been investigated previously. However, since ZPEs can change relative energy differences between the hydrogen isotopes we calculate the binding energy for placements at all inequivalent NOS in the vacancy. Sites indicated in Table VI are defined in the schematic in Figure 4.

To quantify the trapping and to benchmark against previous works, we calculate the incremental binding energy. This measures the binding energy of the n^{th} hydrogen isotope added to a $H_{n-1}V$ complex[132]:

$$E_B^{\text{inc}} = (E(H_{n-1}V) + E(H_{\text{TET}})) - (E(H_nV) + E_0) \quad (24)$$

$E(H_{n-1}V)$ and $E(H_nV)$ are the energies of the bcc iron crystal containing a monovacancy with $n-1$ and n hydrogen isotopes, respectively. All systems have the same volume and include an elastic correction. Where necessary, ZPEs are added to each term which includes hy-

drogen in the configuration. The trapping energies E_B^{inc} and ZPEs are provided in Table VI. In this definition, a positive binding energy identifies an attractive interaction. Our results show good agreement with previous calculations. We also include calculations without the elastic correction for direct comparison with the results in Ref. 132 which used very comparable DFT parameters. ZPE corrections for a H_nV complex ($n=1-4$), ranging between 0.135-0.145eV/H, in Ref. 28 are agreeable with our results.

If molecular hydrogen (H_2) is placed into a vacancy the hybridisation with iron causes the molecule to dissociate and the hydrogen atoms to take NOS on opposite faces of the monovacancy[28]. Three hydrogen take an open structure residing in NOS's on a common [100] plane. Four hydrogen prefer their NOS to form a tetrahedon[26]. However, for deuterium and tritium, a co-planar configuration is calculated to be the lower energy structure in contrast to protium.

When six hydrogen fill a monovacancy, our calcula-

TABLE V. Binding energy (in eV, calculated using Eqn. 23) of two hydrogen isotopes in solution within α -Fe. Initial distance between the pair of hydrogen atoms and the final positions after atomic relaxation are presented in units of the lattice parameter $a=2.832\text{\AA}$. The naming convention (ID) follows Figure 2 of Ref. 88. Binding energies for protium are shown in comparison to calculations from Ref. 88 which used comprable DFT parameters, as well from an interatomic potential (IP) from Ref. 89 (taken from Ref. 123) which was fit to include the ZPE correction.

ID	Initial Distance	Relaxed distance	Magnetic Moments		¹ H			² H	³ H
			H_{fixed}	H_{site}	DFT	DFT	IP	DFT	DFT
					Present	Ref.88	Ref.89	Present	Present
2H2	$\frac{1}{2}a=0.5a$	0.691a	-0.024	-0.024	-0.068			-0.082	-0.088
2H3	$\frac{1}{2}\sqrt{\frac{3}{2}}a=0.612a$	0.663a	-0.024	-0.024	-0.032	-0.032	0.004	-0.037	-0.039
2H4	$\frac{1}{\sqrt{2}}a=0.707a$	0.712a	-0.023	-0.023	0.021	0.023	0.046	0.019	0.019
2H5	$\frac{\sqrt{10}}{4}a=0.791a$	0.807a	-0.024	-0.023	0.007	0.009	0.054	0.006	0.006
2H6	$\frac{\sqrt{3}}{2}a=0.866a$	0.877a	-0.023	-0.023	0.014	0.015	0.038	0.013	0.013
2H7	$\frac{\sqrt{14}}{2}a=0.935a$	0.950a	-0.023	-0.023	-0.000	0.002	0.014	0.000	0.000
2H8a	a	1.002a	-0.024	-0.024	0.020	0.022	0.035	0.019	0.019
2H8b	a	1.015a	-0.023	-0.023	-0.017	-0.014	0.003	-0.017	-0.017
2H9a	$\frac{3}{4}\sqrt{2}a=1.061a$	1.096a	-0.023	-0.023	-0.034	-0.033	-0.018	-0.033	-0.033
2H9b	$\frac{3}{4}\sqrt{2}a=1.061a$	1.112a	-0.022	-0.022	-0.032	-0.030	-0.025	-0.030	-0.030
2H10a	$\frac{\sqrt{5}}{2}a=1.118a$	1.115a	-0.024	-0.024	0.012	0.014	0.024	0.011	0.011
2H10b	$\frac{\sqrt{5}}{2}a=1.118a$	1.178a	-0.022	-0.022	-0.048	-0.047	-0.034	-0.046	-0.045
2H11	$\frac{1}{2}\sqrt{\frac{11}{2}}a=1.173a$	1.174a	-0.023	-0.023	0.009	0.011	0.018	0.008	0.008
2H12	$\sqrt{\frac{3}{2}}a=1.226a$	1.227a	-0.023	-0.023	0.009	0.013	0.018	0.008	0.008

tions indicate that a symmetry broken octahedral cage is formed with four coplanar hydrogen moving towards a tetrahedral site (see Figure 4(b)). The centrosymmetric configuration is found to have negative eigenvalues whose eigenvectors correspond displacements driving the rotation of the cage. This hydrogen arrangement has been noted previously [12, 15]. Unlike in the work by Hayward and Fu, our vibrational analysis did not identify negative eigenvalues for the symmetry broken configuration. In previous results in the literature the binding energy of the symmetry broken configuration is nearly zero[12, 132]. However, our calculations identify that once ZPE is included, it becomes more strongly bound, albeit less so than configurations with fewer hydrogen. We note that is we were to approximate the ZPE for this configuration using the ZPEs of hydrogen in solution, $4ZPE(H_{\text{TET}}) + 2ZPE(H_{\text{OCT}}) \approx 20 \text{ eV}/^1\text{H}$, then the incremental binding energy for the 6th protium would instead be -0.07 eV. This identifies that explicit calculations of ZPE are necessary.

We were unable to find an arrangement for 7 hydrogen atoms which did not have negative eigenfrequencies in the vibrational analysis. Further, for those configurations we did investigate, the trapping energy for the addition of the 7th hydrogen isotope was strongly repulsive.

Due to symmetrically equivalent positions that may be taken by hydrogen atoms trapped in the monovacancy, a useful definition is the average binding energy[12]:

$$E_B^{\text{av}} = \frac{1}{n} \left(E(V) - E(H_n V) \right) + E_{\text{TET}} - E_0 \quad (25)$$

where $E(V)$ is the energy of the monovacancy in the absence of any hydrogen atoms. As noted by Hayward, this is because once the low energy configuration has been adopted, symmetric sites make particular hydrogen indistinguishable so we may no longer say that the x^{th} hydrogen is more or less bound than y^{th} hydrogen added. The average binding then provides a more robust measure of the trapping capacity of a hydrogen-vacancy complex. The average binding energies for each isotope, along with the incremental binding energies, are shown in Figure 5. For protium we show complementary DFT results from Ref. [12] and Ref. [28]. The former used a basis set of linear combination of pseudo-atomic orbitals with the SIESTA code. The latter similarly formed a basis using plane waves but implemented ultrasoft pseudopotentials via the STATE code. All calculations employ the PBE exchange-correlation functional and spin-polarisation but have different system sizes. Each DFT method shows that a monovacancy with two protium atoms on opposite faces are the most strongly bound. Our results agree with Ref. [12] predicting that additional protium are successively less bound. This is in contrast to Ref. [28] which determined a small jump in binding energy for the H_4V complex. This may be a result of internal stresses from the small simulation size used.

For deuterium we may compare directly with ion-beam experiments[1, 2] and a theoretical effective-medium theory[1, 58]. In the ion beam experiment, once the all deuterium had been trapped, two deuterium desorption stages were detected at 0.43 eV and 0.63 eV. The 0.63 eV stage is in good quantitative agreement with the binding energies for one (0.65 eV) and two (0.67 eV) deuterium

TABLE VI. Incremental binding energy (in eV, Eqn. 24), average binding energy (in eV, Eqn. 25) and dissolution energy (in eV, Eqn. 26, also referred to as trapping energy) of hydrogen isotopes trapped within a monovacancy in bcc Fe. Sites (a-g) are defined in Fig. 4 and represent the initial placement of hydrogen (most configurations have symmetrically equivalent alternative placements). Comparative data from references [132] and [12] are also DFT calculations. The ZPE correction for protium is presented in units eV/ n , where n is the number of hydrogen atoms in the simulation cell. We provide incremental binding energies for calculations at fixed volume (FV) and full cell relaxation (RC.). ZPE corrections are applied to the fixed volume energies. Daggered IDs indicate configurations which have negative eigenvalues in the vibrational analysis and therefore are not true minima.

n	ID	Sites	H				¹ H		² H	³ H	
			Present (FV)	Present (RC)	Ref.132	Ref.12	ZPE/ n_H	Present	Ref.12	Present	Present
Incremental binding energy											
1	1V1H	a	0.581	0.584	0.584	0.498	0.139	0.681	0.616	0.651	0.638
2	1V2H	af	0.604	0.605	0.607	0.543	0.140	0.701	0.651	0.673	0.660
2	1V2Hb	ab	0.511	0.513			0.157	0.574		0.555	0.547
3	1V3H	abc	0.399	0.401	0.384	0.337	0.157	0.446	0.381	0.433	0.427
3	1V3Hb	abd	0.354	0.355			0.162	0.387		0.378	0.373
4	1V4H	abcf	0.288	0.287			0.141	0.434		0.391	0.372
4	1V4Hb	abcd	0.359	0.359	0.343	0.304	0.164	0.414	0.351	0.398	0.391
5	1V5H	abcde	0.300	0.298	0.297	0.269	0.175	0.300	0.269	0.314	0.311
6	1V6H [†]	abcdef	0.030	0.027	0.002		0.145	0.271		0.201	0.169
6	1V6Hb	abcdef	0.032	0.029	0.045	-0.043	0.159	0.188	0.045	0.142	0.122
7	1V7H [†]	abcdefg	-2.442	-2.449			0.155	-2.134		-2.223	-2.263
Average binding energy											
1	1V1H	a	0.581				0.139	0.681	0.62	0.651	0.638
2	1V2H	af	0.593				0.140	0.691	0.63	0.662	0.649
2	1V2Hb	ab	0.546				0.157	0.627		0.603	0.593
3	1V3H	abc	0.528				0.157	0.609	0.55	0.586	0.575
3	1V3Hb	abd	0.513				0.162	0.590		0.567	0.557
4	1V4H	abcf	0.468				0.141	0.565		0.537	0.524
4	1V4Hb	abcd	0.486				0.164	0.560	0.50	0.539	0.529
5	1V5H	abcde	0.449				0.175	0.512	0.45	0.494	0.486
6	1V6H [†]	abcdef	0.379				0.145	0.472		0.445	0.433
6	1V6Hb	abcdef	0.379				0.159	0.458	0.39	0.435	0.425
7	1V7H [†]	abcdefg	-0.024				0.155	0.100		0.064	0.048
Average dissolution energy											
1	1V1H	a	-0.376				0.139	-0.375	-0.39 ^a	-0.375	-0.375
2	1V2H	af	-0.387				0.140	-0.385	-0.40 ^a	-0.386	-0.386
2	1V2Hb	ab	-0.341				0.157	-0.321		-0.327	-0.330
3	1V3H	abc	-0.323				0.157	-0.303	-0.32 ^a	-0.309	-0.312
3	1V3Hb	abd	-0.308				0.162	-0.284		-0.291	-0.294
4	1V4H	abcf	-0.263				0.141	-0.260		-0.261	-0.261
4	1V4Hb	abcd	-0.281				0.164	-0.255	-0.27 ^a	-0.262	-0.266
5	1V5H	abcde	-0.244				0.175	-0.207	-0.22 ^a	-0.217	-0.222
6	1V6H [†]	abcdef	-0.174				0.145	-0.167		-0.169	-0.169
6	1V6Hb	abcdef	-0.174				0.159	-0.152	-0.16 ^a	-0.159	-0.162
7	1V7H [†]	abcdefg	0.229				0.155	0.206		0.213	0.216

^a Calculated from values in Tables II and VI of Ref. 12 using Eqn. 26.

atoms in a monovacancy. The 0.43 eV stages matches the average binding energy for 6 deuterium vacancy complex. If we consider that the binding energies of deuterium are typically 20-30meV lower than protium, then we note that our results are typically overbound relative to experiment, whereas results in Ref. [12] are underbound.

The n^{th} hydrogen may be considered to be exothermi-

cally bound to the complex if its binding energy is greater than the heat of solution of the hydrogen molecule. That is, its average energy of dissolution is negative:

$$E_d^{\text{av}} = E_{\text{sol}}^{\text{TET}} - E_B^{\text{av}} \quad (26)$$

The heats of solution for each isotope are given in Table II. Note, this is formally equivalent to the dissolution

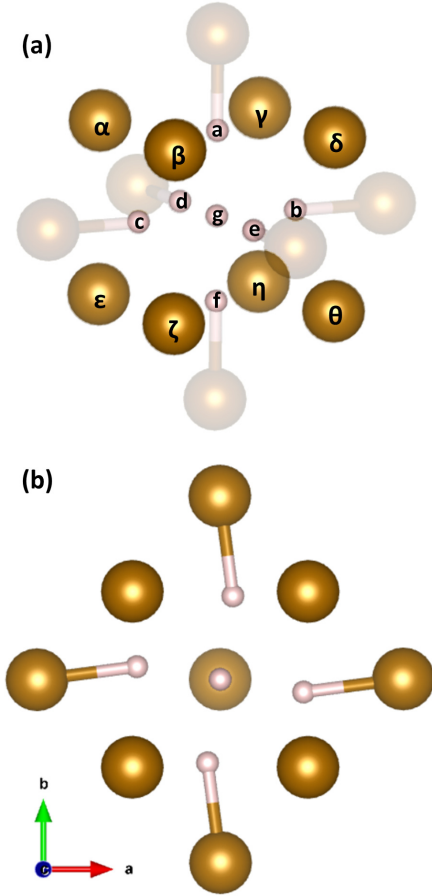


FIG. 4. (a) Schematic defining initial NOS positions of hydrogen within a mono-vacancy. (b) Cross section on a (001) plane of the non-centrosymmetric relaxed configuration 6B.

energy defined in Ref. 59. In Figure 5 the endothermic region is highlighted by grey shading. Our calculations for the heavy hydrogen isotopes, up to 4 hydrogen are clearly exothermically bound relative to the incremental binding energy. The 5th is just exothermic whereas the 6th is endothermic. However, for protium the addition of the 5th to the protium-vacancy complex is slightly endothermic. Since the heavier isotopes are more exothermically bound (greater magnitude of dissolution energy) they will have a greater propensity to be trapped to a vacancy. We may then propose that since protium has a higher diffusivity in the bulk and is less exothermically bound, that as heavier isotopes approach a vacancy they will replace protium atoms in the complex. However, the difference in the dissolution energies of the isotopes are typically within 10 meV so these kinetic isotope effects may be negligible in practicality at room temperature.

Finally we may consider vacancy formation due to hydrogen saturation. The notion of super-abundant vacancy formation has been proposed and observed in several metal-hydrogen alloys[52, 55]. The formation energy of a vacancy in the vicinity of n hydrogen isotopes may

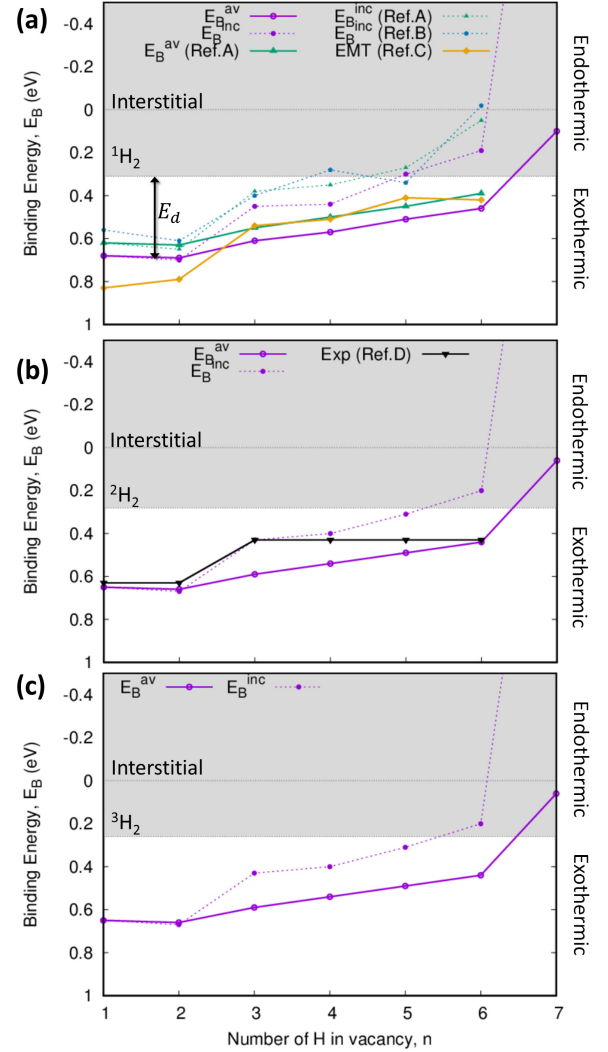


FIG. 5. Incremental (Eqn. 24, dashed) and average (Eqn 25, solid) binding energies for n (a) protium (b) deuterium or (c) tritium trapped within a mono-vacancy in bcc iron. The energy of the hydrogen isotope in an interstitial site (origin) and as a ${}^n\text{H}_2$ molecule in vacuo are indicated. The difference between the binding energy and the energy of the energy of the molecule corresponds to the dissolution/trapping energy. We present our results (purple) compared to DFT data from Refs. [12] (Ref.A) and [28] (Ref.B) and effective medium theory (EMT) from Ref. [58] (Ref.C). Experimental desorption stages for deuterium (0.63eV, 0.43eV) are from Ref [1] (Ref.D).

be approximated using[12]:

$$E_f^{H_n V} = E(H_n V) - \frac{N-1}{N} E_0 - n(E(H_{TET}) - E_0) \quad (27)$$

where N is the number of Fe atoms in the perfect cell (250 for these calculations). The results for each isotope are shown in Figure 6.

The formation energy decreases as the hydrogen-vacancy complex traps more hydrogen becoming negative when $n > 4$. Once ZPEs are included, protium

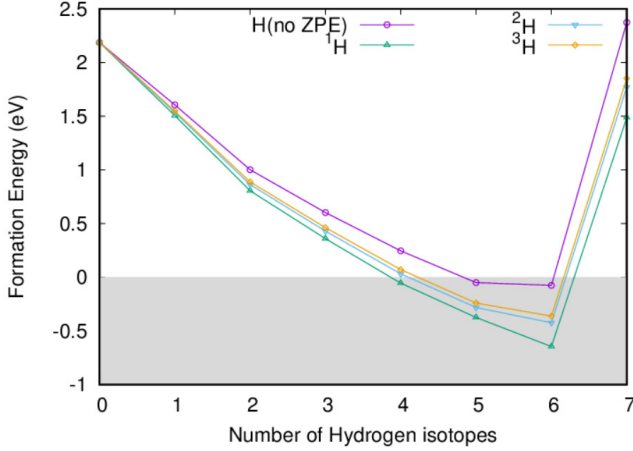


FIG. 6. Formation energy (Eqn. 27) of a vacancy trapping multiple hydrogen isotopes.

has the smallest vacancy formation energy. These results may provide an explanation as to why hydride formations have not been experimentally observed at low hydrogen pressure despite the small formation energies[125, 126]. When the local hydrogen concentration is high, due to the negative formation energy of concentrated H_nV complexes, it may be energetically preferable to form to vacancy-hydrogen complex rather than precipitate into a hydride cluster.

2. The effect of Cr on the efficacy of vacancy trapping

The deleterious effect of vacancies trapping hydrogen atoms may be altered in the presence of Cr. Substituting a Cr atom in place of one of the Fe atoms which are nearest neighbour to the vacant site has a binding energy of 0.050 eV which is in good agreement with Olssons value of 0.057 eV[133]. Since the interaction is attractive we consider its ability to trap hydrogen isotopes. We modify the calculation of incremental binding energy to account for the Cr atom using an analogous approach to Eqn. 24:

$$E_B^{\text{inc}} = \left(\min[E(H_{n-1}Cr_{Fe}V)] + E(H_{\text{TET}}) \right) - \left(E(H_nCr_{Fe}V) + E_0 \right) \quad (28)$$

where $E(H_nCr_{Fe}V)$ is the energy of the system containing n hydrogen within a vacancy that has a Cr atom in one of the eight sites surrounding the vacancy. Since the Cr reduces the symmetry of the system, $\min[E(H_{n-1}Cr_{Fe}V)]$ is the energy of the configuration with one fewer hydrogen atoms which has the lowest energy. Similarly we may redefine the average binding and

dissolution energies to account for the Cr solute:

$$E_B^{\text{av}} = \frac{1}{n} \left(E(CrV) - E(H_nCrV) \right) + E^{\text{TET}} - E_0 \quad (29)$$

$$E_d^{\text{av}} = E_{\text{sol}}^{\text{TET}} - E_B^{\text{av}} \quad (30)$$

The binding and dissolution energies are given in Table VII. In most cases we only considered the lowest energy configurations for the hydrogen-vacancy complexes for Cr substitution. For two hydrogen isotopes we considered both the open and closed configurations. Schematics of the Cr-H-V complexes following energy minimisation are presented in Figure 7. In the bulk, Cr was shown to repel hydrogen in solution. The same effect is observed for the vacancy complexes. Hydrogen isotopes near the Cr substitution are pushed from *near octahedral sites* towards tetrahedral positions such that they inhabit sites between the octahedral and tetrahedral interstitial sites.

Unlike in pure iron where a pair of hydrogen isotopes are most strongly bound, if Cr is present then the binding is most attractive for a single hydrogen isotope with the attraction getting weaker for each successive hydrogen trapped. Whilst the binding energy is lower for the first hydrogen to be trapped, the binding is stronger for the 5th and 6th hydrogen relative to a vacancy without a neighbouring Cr. These results may be interpreted as an elastic effect. The relaxation volume of a vacancy is -2.39\AA^3 , indicating the atoms shrink into the vacancy. When the Cr atom is included the relaxation volume of the complex is -0.36\AA^3 clearly identifying the volume of the vacancy is larger providing more room for the trapped hydrogen. Nonetheless a seventh hydrogen is still found to be unfavorable. The relaxation volumes of the lowest energy configurations for one or two hydrogen in the Cr free vacancy are -1.20\AA^3 and 0.50\AA^3 , respectively. With Cr, the relaxation volumes for one or two hydrogen in low energy configurations are 1.01\AA^3 and 2.56\AA^3 , respectively. In both cases, the configurations whose relaxation volumes are closest to zero (indicating minimal stress on the simulation cell and a volume of the complex comparable to the iron host atom) have the most attractive binding. The dissolution energy is greater as the mass of the hydrogen isotope increases. However, as observed for the vacancy in the absence of Cr, the differences are typically within 10 meV.

Magnetic moments of the transition metals are additionally provided in Figure 7. The moment of Cr neighbouring the vacancy is substantially larger than either its bulk value or even its magnitude when substituted into the bulk. When no hydrogen are present in the vacancy the Cr has a magnetic moment of $-2.10\mu_B$ which is in good agreement with comparable calculations (eg. $-1.99\mu_B$ in Ref. 133 which also used PAW pseudopotentials but a smaller simulation cell). When there are relatively few hydrogen atoms trapped in the vacancy, the magnetic moment of the Cr is reduced if a hydrogen is near a NOS neighbouring it. If the hydrogen are on the other side of the vacancy, the Cr moment is increased.

TABLE VII. Incremental binding energy (in eV, Eqn. 28), average binding energy (in eV, Eqn. 29) and dissolution energy (in eV, Eqn. 30, also referred to as trapping energy) of hydrogen isotopes trapped within a monovacancy in bcc Fe with a Cr substitution in a first nearest neighbouring site to the vacancy. Sites a-g are defined in Fig. 4 and represent the initial placement of hydrogen and sites $\alpha - \theta$ represent the placement of Cr. The ZPE correction for protium is presented in units eV/ n , where n is the number of hydrogen atoms in the simulation cell. Daggered IDs indicate configurations which have negative eigenvalues in the vibrational analysis and therefore are not true minima.

ID	n_H	Cr site	H sites	H	ZPE/ n_H	^1H	^2H	^3H
Incremental binding energy								
1V1Cr1H	1	α	a	0.539	0.145	0.632	0.605	0.593
1V1Cr1Hb	1	ϵ	a	0.583	0.137	0.684	0.654	0.641
1V1Cr2H	2	α	af	0.554	0.142	0.644	0.618	0.606
1V1Cr2HB	2	α	ae	0.439	0.159	0.496	0.479	0.472
1V1Cr2HBb	2	δ	ae	0.449	0.162	0.501	0.486	0.479
1V1Cr2HBc	2	ϵ	ae	0.516	0.156	0.632	0.607	0.597
1V1Cr3H	3	α	ade	0.372	0.164	0.403	0.394	0.390
1V1Cr3Hb	3	η	ade	0.373	0.157	0.425	0.409	0.403
1V1Cr4H	4	α	adef	0.267	0.156	0.355	0.329	0.318
1V1Cr5H	5	ϵ	abcde	0.293	0.171	0.301	0.299	0.298
1V1Cr5Hb	5	α	abcde	0.368	0.179	0.332	0.343	0.347
1V1Cr6H [†]	6	α	abcdef	-0.031	0.150	0.201	0.133	0.103
Average binding energy								
1V1Cr1H	1	α	a	0.539	0.145	0.632	0.605	0.593
1V1Cr1Hb	1	ϵ	a	0.583	0.137	0.684	0.654	0.641
1V1Cr2H	2	α	af	0.568	0.142	0.664	0.636	0.624
1V1Cr2HB	2	α	ae	0.511	0.159	0.590	0.567	0.556
1V1Cr2HBb	2	δ	ae	0.516	0.162	0.592	0.570	0.560
1V1Cr2HBc	2	ϵ	ae	0.549	0.156	0.632	0.607	0.597
1V1Cr3H	3	α	ade	0.503	0.164	0.577	0.555	0.546
1V1Cr3Hb	3	η	ade	0.503	0.157	0.584	0.560	0.550
1V1Cr4H	4	α	adef	0.444	0.156	0.527	0.503	0.492
1V1Cr5H	5	ϵ	abcde	0.414	0.171	0.482	0.462	0.453
1V1Cr5Hb	5	α	abcde	0.429	0.179	0.488	0.471	0.463
1V1Cr6H [†]	6	α	abcdef	0.352	0.150	0.440	0.414	0.403
Average dissolution energy								
1V1Cr1H	1	α	a	-0.334	0.145	-0.326	-0.328	-0.329
1V1Cr1Hb	1	ϵ	a	-0.377	0.137	-0.378	-0.378	-0.378
1V1Cr2H	2	α	af	-0.363	0.142	-0.358	-0.360	-0.360
1V1Cr2HB	2	α	ae	-0.306	0.159	-0.284	-0.290	-0.293
1V1Cr2HBb	2	δ	ae	-0.311	0.162	-0.287	-0.294	-0.297
1V1Cr2HBc	2	ϵ	ae	-0.344	0.156	-0.326	-0.331	-0.334
1V1Cr3H	3	α	ade	-0.298	0.164	-0.271	-0.279	-0.282
1V1Cr3Hb	3	η	ade	-0.298	0.157	-0.278	-0.284	-0.287
1V1Cr4H	4	α	adef	-0.239	0.156	-0.221	-0.226	-0.229
1V1Cr5H	5	ϵ	abcde	-0.209	0.171	-0.176	-0.185	-0.190
1V1Cr5Hb	5	α	abcde	-0.224	0.179	-0.182	-0.194	-0.200
1V1Cr6H [†]	6	α	abcdef	-0.147	0.150	-0.134	-0.138	-0.140

When there are four or more hydrogen, the reverse effect is noted with the Cr moment even greater when there is a saturation of hydrogen in the NOS around it. The magnetic moments of the hydrogen remain small (-0.2 to $-0.3\mu_B$). Hydrogen which have the greatest displacement from NOS have the larger magnetic moments.

The valency of Cr ($[\text{Ar}]3d^54s^1$) is less than iron ($[\text{Ar}]3d^64s^2$) such that the charge density in the volume complex will be reduced. In metals, hydrogen preferentially situates where the charge density is low[134, 135]

meaning we would expect a reduction in the dissolution energy. Indeed, relative to equivalent hydrogen configurations in the vacancy without the neighbouring Cr atom we observe a small reduction in the dissolution energy.

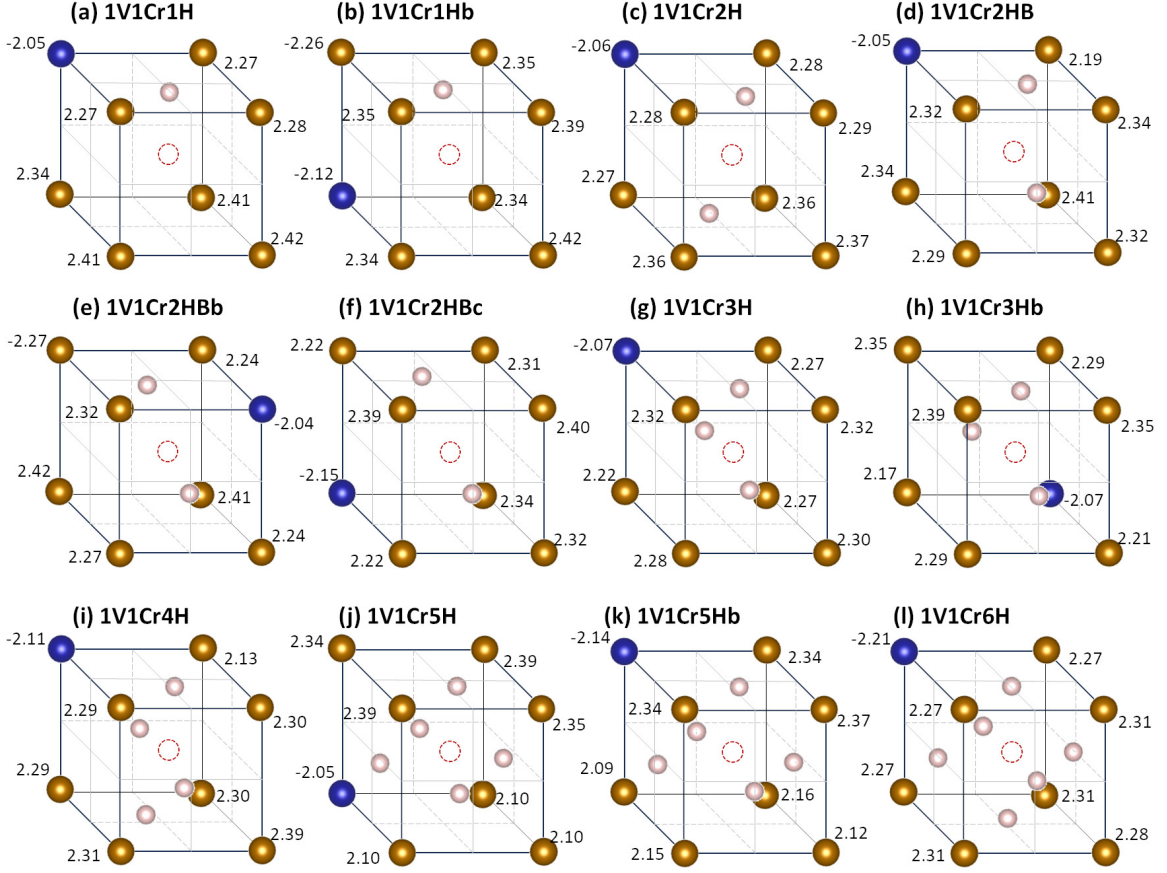


FIG. 7. Relaxed positions and local magnetic moments of the $\text{Cr}\square\text{H}_n$ complex. Magnetic moments of the hydrogen isotopes are not shown for brevity. Hydrogen moments near octahedral sites have moments close to $-0.02\mu_B$ whilst those which are displaced have increased magnetic moments upto $-0.03\mu_B$. All magnetic moments are in units of the Bohr magneton μ_B .

C. Binding of hydrogen isotopes to $\langle 110 \rangle$ Self Interstitial Atoms in α -Fe

In this section we analyse whether the any hydrogen isotopes will be trapped by self-interstitial atoms (SIA) in the iron matrix. We limit our calculations to sites in the conventional unit cell which contains the SIA at its center and are shown in Figure 8. As magnetism results in the stabilisation of a $\langle 110 \rangle$ dumbbell in α -Fe[41?] this is the SIA configuration we decorate. We confirm our DFT calculations predict the correct order of stability for SIAs of $\langle 110 \rangle \rightarrow$ Tetrahedral (0.46 eV) \rightarrow $\langle 111 \rangle$ (0.73 eV) \rightarrow $\langle 100 \rangle$ (1.11 eV) \rightarrow Octahedral (1.24 eV), where the bracketed values indicate the relative energy to the $\langle 110 \rangle$ which has a formation energy of 3.94 eV.

The binding energy between the SIA and a hydrogen interstitial can be approximated as:

$$E_b^{\text{SIA}+\text{H}} = E(H_{\text{TET}}) + E(\text{SIA}) - E(\text{SIA} + H_{\text{TET}}) - E_0 \quad (31)$$

where $E(\text{SIA} + H_{\text{TET}})$ and $E(\text{SIA})$ are the energies of systems containing an iron interstitial in a $\langle 110 \rangle$ dumb-

bell configuration, with and without a hydrogen isotope, respectively. These cells contain 251 Fe atoms, compared to E_0 which is the perfect iron cell which contains 250 atoms. In this formulation, a positive binding energy reflects an attractive interaction. Results are presented in Table VIII.

As to be expected, where volume is limited due to the coexistence of an SIA and hydrogen isotope, the interactions are repulsive or result in the ejection of the hydrogen from the complex. Heavier hydrogen isotopes have stronger repulsive interactions that protium. In the tensile site (8), hydrogen is weakly bound, with the interaction weakening as the isotope mass increases.

Magnetic effects are known to change the order of SIA stability relative to other bcc transition metals. For instance, the $\langle 111 \rangle$ dumbbell/crowdion has a mixed e_g - t_{2g} characteristic of the bands at the Fermi energy which has non-Heisenberg interactions increasing the relative energy of the configuration[?]. To see if magnetic states are affected we also examine the change in magnetisation in the defect core. Without hydrogen, our DFT calculations predict the moments to have a magnitude of $0.2\mu_B$ oriented antiparallel to the magnetisation axis.

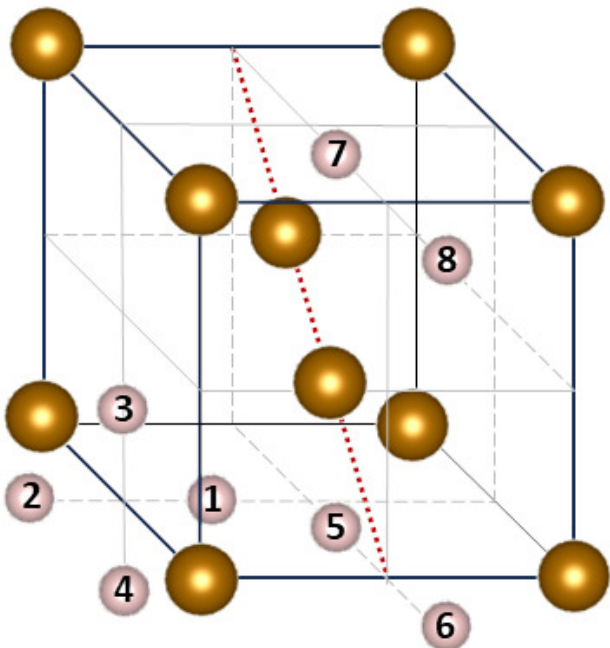


FIG. 8. Schematic detailing the tetrahedral sites chosen to position a hydrogen atom adjacent to an iron SIA. The SIA is constructed as a $\langle 110 \rangle$ dumbbell.

Spin lattice dynamics simulations including both longitudinal and transverse fluctuations of the magnetic moment have shown this property to persist with lattice fluctuations and temperature[45]. The presence of hydrogen is shown to break the symmetry of the core moments. Tetrahedral sites which are most repulsive have typically caused the magnetisation of one of the core iron atoms to flip or significantly quenched (Table VIII).

D. Surfaces

1. Adsorption of hydrogen isotopes on iron surfaces

Iron surfaces are known to dissociately absorb hydrogen in a strongly exothermic process[15, 136–140]. The chemisorbed hydrogen can then diffuse into the sublayers and then into the bulk, or from the bulk to the surface[11]. We investigate the adsorption of hydrogen isotopes on the (100) and (110) low index surfaces which are the most stable clean surface terminations for iron[141]. We generated slabs with approximately 12Å of vacuum between surface terminations, comprised of 10 (for (100)) and 12 (for (110)) layers which satisfied convergence of properties. Due to the magnetic moment of iron which arises from the asymmetric filling of 3d bands, we fix the positions of iron atoms in the two layers at the center of the slab. This is found to ensure the iron atoms at the center of the slab were 'bulk-like'. Fixing the positions of atoms at one surface leads to erroneous enhanced

magnetic moments of the 'bulk-like' atoms despite the ideal lattice constant, whose magnetic interactions then interfere with the relaxation of iron atoms in the rest of the slab (see Figure 9).

In the absence of hydrogen, the surface energies from our calculations are 2.41 Jm^{-2} and 2.48 Jm^{-2} for the (110) and (100) surfaces, respectively. The surface energy is calculated using:

$$\gamma_{[hkl]} = \frac{E_{\text{slab}}^{[hkl]} - E_0}{2A} \quad (32)$$

where $E_{\text{slab}}^{[hkl]}$ is the energy of the system with a (100) or (110) surface termination, E_0 is the energy of bulk bcc iron with an identical number of atoms to the surface system, and A is the surface area. Our surface energies are in good agreement with previous calculations which also determine the (110) surface to be the lowest energy (see Table IX).

High symmetry absorption sites for both surface terminations are shown in Figure 10. We construct the simulation cells to be asymmetric (placement of hydrogen on one surface only). We confirmed calculated results are identical to a symmetric construction or the use of a dipole correction.

The adsorption energy can then be calculated as:

$$E_{\text{ads}}^{[hkl]} = E_{\text{slab}}^{[hkl]}(H) - E_{\text{slab}}^{[hkl]} - \frac{1}{2}E(H_2) \quad (33)$$

where $E_{\text{slab}}^{[hkl]}(H)$ is the energy of an iron slab with hydrogen adsorbed on a surface site. In this definition, a negative adsorption energy corresponds to adsorbate binding. By subtracting the heat of solution of hydrogen ($E_{\text{sol}}^{\text{TET}}$) from the adsorption energy a *binding energy* may be defined[89]:

$$E_b^{\text{surface+h}} = E_{\text{sol}}^{\text{TET}} - E_{\text{ads}} \quad (34)$$

Adsorption and binding energies for hydrogen isotopes on the lower energy (110) surface termination are provided in Table X as a function of surface coverage (Θ). In this work, the surface coverage is defined as the ratio between the number of surface metal atoms to the number of adsorbate atoms[11]. Our calculations identify the same order of stability for hydrogen adsorption being quasi-threefold \rightarrow long-bridge (0.06eV, 0.06eV[145]) \rightarrow short-bridge (0.17eV, 0.18eV[145]) \rightarrow on-top (0.70eV, 0.75eV[145]), where the values bracketed values provide the adsorption energies relative to the quasi-threefold site before ZPE has been applied. Vibrational analysis is also consistent with other calculations identifying only the quasi-threefold site to be a true minimum[21]. The long-bridge and short-bridge sites have one negative eigenvalue indicating they are transitional states. The on-top site has two non-degenerate negative eigenvalues which identifies it as being a rank 2 saddle point. The adsorption of hydrogen to the quasi-threefold site has been experimentally verified at various covering fractions and

TABLE VIII. Binding energy (in eV, calculated using Eqn. 31) and magnetic moments (in μ_B) for hydrogen atoms decorating a $\langle 110 \rangle$ dumbbell in α -Fe. The magnetic moments M_1 and M_2 are for iron atoms in the core of the SIA, where M_1 is the core atom closest to the hydrogen interstitial. The magnetic moments of iron atoms in the core without hydrogen are both $-0.192\mu_B$. Hydrogen positions for each ID are defined in Figure 8.

ID	Site	Binding energy (eV)					Magnetic moment (μ_B)			
		H	ZPE	^1H	^2H	^3H	M_1	M_2	M_H	
$\langle 110 \rangle H1$	1				Becomes config ID=4					
$\langle 110 \rangle H2$	2	-0.036	0.224	-0.022	-0.026	-0.028	-0.021	-0.194	-0.023	
$\langle 110 \rangle H3$	3	-0.131	0.207	-0.100	-0.109	-0.113	+0.148	-0.242	-0.018	
$\langle 110 \rangle H4$	4	-0.041	0.207	-0.010	-0.019	-0.023	+0.089	-0.152	-0.021	
$\langle 110 \rangle H5$	5				Unstable. H ejected.					
$\langle 110 \rangle H6$	6	-0.077	0.213	-0.051	-0.059	-0.062	+0.200	-0.275	-0.019	
$\langle 110 \rangle H7$	7	-0.156	0.223	-0.144	-0.148	-0.149	-0.203	+0.134	-0.020	
$\langle 110 \rangle H8$	8	0.014	0.232	0.021	0.019	0.018	-0.138	-0.116	-0.025	

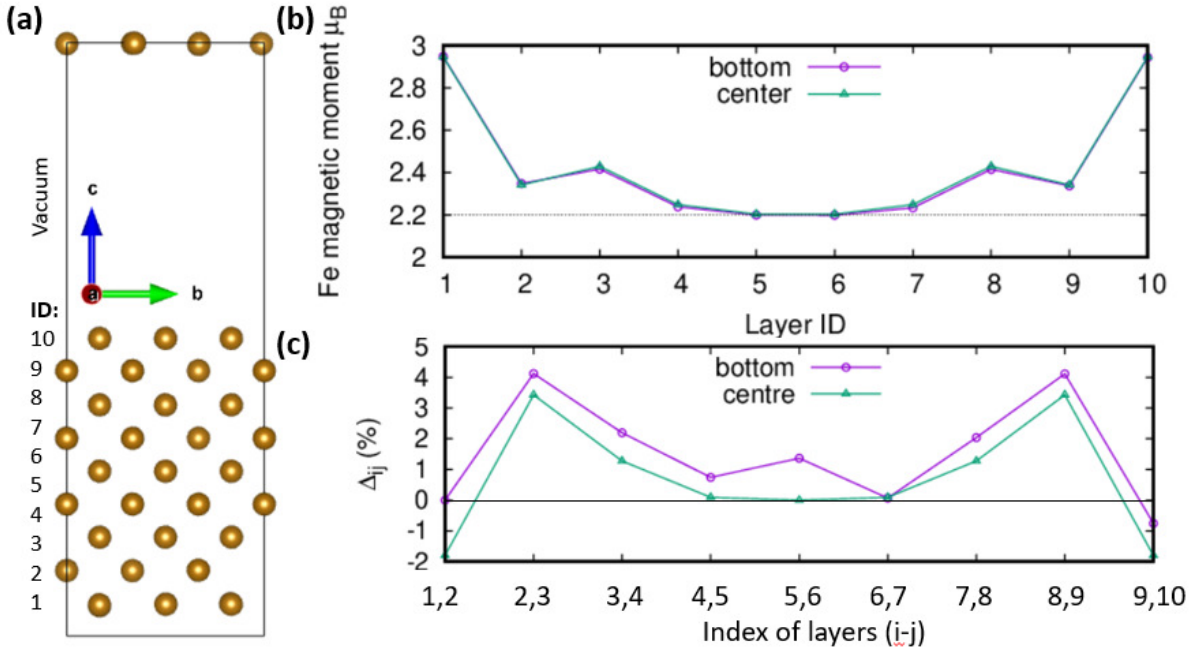


FIG. 9. Erroneous properties of Fe films with fixed surface atoms. (a) Schematic of a slab with a clean (001) p(3 × 3) surface termination with 12Å vacuum region. (b) Spontaneous magnetic moments of iron atoms as function of interatomic layer in the slab. The magnetic moment of iron in bulk is $2.2\mu_B$ shown as the dashed line. Whether the central two layers (ID=5,6) or two surface layers (ID=1,2 or ID=9,10) are fixed, there is strong enhancement of magnetic moments at the surface showing substantial change to electronic structure of surface atoms whether positions at ideal lattice parameter or free to relax. (c) Relative change in interatomic spacing between layers Δ_{ij} relative to bulk. When the bottom layers are fixed (ID=1,2) to represent bulk-like atoms, an unphysical interatomic spacing is observed with the next sublayer (ID=2,3) due to the large magnetic moments of these surface (and 1st subsurface) atoms. When the central layers are fixed, their magnetic moments are bulk-like and there is a smooth change in the interatomic spacing towards each surface. For the centrally fixed slab, $\Delta_{12} = -1.8\%$ in reasonable agreement with the experimental value of $-1.4 \pm 0.3\%$ [142].

phases[140, 146, 147]. Application of ZPE from the hydrogen vibrational modes retains the order of stability for each isotope. Electron energy loss spectroscopy at room temperature and covering fraction $\Theta = 0.25$ has shown the symmetric stretch frequency to be 1060 cm^{-1} [148], which is comparable to the frequency 1077 cm^{-1} our calculations predict for the same Θ in the p(2 × 1) phase. This difference equates to 2 meV and is within the ex-

pected error of DFT calculations. The binding energies show the surface interaction is diminished for deuterium and tritium relative to protium.

For the (100) surface the adsorption and binding energies are presented in Table XI. Our results are in agreement with previous DFT calculations which identify the Hollow site as the most bound for low covering fractions[11, 89, 145]. Before zero point energies are ap-

TABLE IX. Surface energies of clean low index surface terminations. Surface energies calculated using Eqn. 32 and presented in units of Jm^{-2}

Surface	Present	DFT	Exp.
110	2.41	2.43 ^a , 2.45 ^b	2.41 ^c
100	2.48	2.50 ^b , 2.49 ^d	

^a Ref. 21

^b Ref. 141

^c Ref. 143

^d Ref. 144

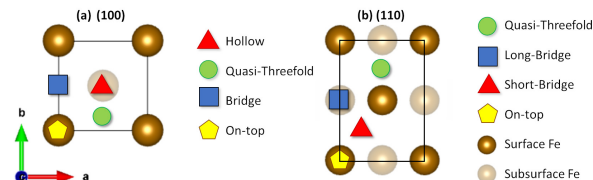


FIG. 10. Schematic of hydrogen adatom sites for orthogonal (100) and (110) terminated Fe surfaces.

plied, at $\Theta = 0.11$, the hollow, quasi-threefold and bridge sites have near degeneracy and are true minima. The on-top site is a second order saddle point. For each covering fraction we get excellent agreement with the results of Jiang and Carter[11] with the notable exception that the adsorption energies in our work are consistently lower in energy and comparable to the hollow site. Comparable adsorption between these two sites was similarly noted for DFT calculations using ultra-soft pseudopotentials[145].

For the higher coverage of $\Theta = 0.25$ our results excellently agree with Ref. 150. In that case, the authors used similar DFT conditions but implemented mirror symmetry about the center of the slab without fixing any layers. In other DFT calculations, atoms at the surface are fixed, however as noted the electronic structure of these atoms will not be ‘bulk-like’ resulting in an energy penalty. The magnetic moments of the surface iron atoms neighbouring the hydrogen adatom are reduced by 4% which agrees with the 3% reduction calculated in Ref. 150.

At a high coverage of $\Theta = 1.0$, our calculations still indicate the hydrogen adatoms will occupy the hollow site. However, experimental evidence using a combination of electron energy loss spectroscopy and temperature programmed desorption indicates the asymmetric quasi-threefold site becomes preferable for saturation coverages due to appearance of high frequency loss at around 1000cm^{-1} [152]. At a coverage of $\Theta = 0.11$ our vibrational analysis for protium gives the mode oscillating towards the short-bridge from the quasi-threefold site to be 1094cm^{-1} . However, at saturation coverage ($\Theta = 1$) we found the frequency to increase to 1240cm^{-1} . The mode oscillating between the hollow and long-bridge sites has a frequency of 991cm^{-1} .

As noted by Ramasubramaniam[89], application of the ZPE correction spreads the range of binding energies.

However, for protium we find this leads to a difference in adsorption energies between the hollow and bridge sites of 0.04 eV opposed to 0.12 eV in their calculations. We find that the binding energy decreases for the heavier hydrogen isotopes. Nonetheless, regardless as to whether hydrogen is adsorbed onto the hollow or quasi-threefold sites, the maximum relative energy difference between the isotopes is merely 10meV or 15meV between protium and deuterium or tritium, respectively. This is consistent with electron energy loss spectroscopy by Merrill and Madix which did not detect an appreciable kinetic isotope effect between the adsorption of protium and deuterium molecules[152].

2. Enhanced adsorption of hydrogen isotopes on (100) Fe surfaces due to subsurface Cr

It should be expected that Cr will modify the adsorption capability of clean surfaces. Indeed, work by Gupta identified that Cr in the surface made the adsorption more exothermic[150] whilst subsurface Cr reduced the adsorption energy. In this work we investigate as to whether the presence of Cr stabilises other sites for a hydrogen adatom and the relative stability for different hydrogen isotopes.

We limit our investigation to surface and subsurface substitutions of Cr only in a $p(3\times 3)$ construction so we may consider the Cr to be reasonably isolated. This equates to a concentration of 1.1%. As for the previous case, our (001) terminated slab consists of 10 layers. We begin by considering the segregation energy of Cr in the absence of any adatoms to check consistency of our calculations. The energy of segregation of the surface layer (SL) is considered to be the energy released when a Cr atom is moved from a lattice site in the subsurface layer (SSL) to a surface site[153]:

$$E_{\text{seg}}^{\text{SSL}\rightarrow\text{SL}} = E_{\text{slab}}(\text{Cr in SSL}) - E_{\text{slab}}(\text{Cr in SL}) \quad (35)$$

Our calculations determine the segregation energy at the surface layer to be 0.292 eV . This can be compared to results by Kuronen *et al* which produced values of 0.251 eV and 0.216 eV for 8 and 12 layer slabs, respectively, using the exact muffin-tin orbital method. The magnetic moment integrated over the PAW sphere for the Cr atom is calculated to be $-3.29\mu_B$ and $-2.18\mu_B$ in the surface and subsurface sites. Substantial increases in the magnetic moment are agreeable with previous work such as in Ref. 150 which reported $-3.10\mu_B$ and $-1.8\mu_B$ for a $p(2\times 2)$ slab with 8 layers, or $-3.13\mu_B$ and $-1.98\mu_B$ in Ref. 144.

Next we consider symmetrically unique sites for a Cr substitution when hydrogen is adsorbed into either a hollow or bridge site. For a hydrogen at a fixed location, the positions of the chosen Cr sites are shown and numbered in the schematic in Figure 7. As the hollow site had 4-fold symmetry relative to the bridges 2-fold, there are fewer unique sites if the hydrogen is in a bridge site.

TABLE X. Adsorption (in eV, Eqn. 33) and binding (in eV, Eqn. 34) energies of hydrogen isotope adatoms on a clean (110) terminated surface of bcc iron. All calculations are performed with a covering fraction (hydrogen per surface metal atom) $\Theta = 0.11$ using a non-orthogonal unit cell. Daggered IDs indicate configurations which have negative eigenvalues in the vibrational analysis and therefore are not true minima.

	Absorption Energy (eV)				
	H(no ZPE)		^1H	^2H	^3H
	DFT	DFT	DFT	DFT	DFT
$\Theta = 0.11$					
Long bridge [†]	-0.618	-0.63 ^a	-0.620	-0.620	-0.619
Short bridge [†]	-0.504	-0.51 ^a	-0.490	-0.494	-0.496
Quasi-threefold	-0.673	-0.69 ^a	-0.640	-0.650	-0.654
Top [†]	+0.023	+0.06 ^a	-0.007	0.002	0.006
	Binding Energy (eV)				
	H(no ZPE)	^1H		^2H	^3H
	DFT	DFT	DFT (Exp)	DFT	DFT
$\Theta = 0.11$					
Long bridge [†]	0.825	0.928	0.970 ^b	0.896	0.883
Short bridge [†]	0.711	0.798	0.823 ^b	0.770	0.759
Quasi-threefold	0.880	0.946	1.003 ^b , (0.86 ^c)	0.926	0.917
Top [†]	0.184	0.313		0.274	0.257

^a Ref.145

^b Ref.89. $\Theta=0.08$ (orthogonal $p(2 \times 2)$ 110 surface construction)

^c Experimental result from Ref.149

The modified heat of adsorption, for a Cr substitution in layer $i=SL$ or $i=SSL$ is:

$$E_{\text{ads}} = E_{\text{slab}}(\text{Cr}_{\text{Fe}}^i \text{H}) - E_{\text{slab}}(\text{Cr}_{\text{Fe}}^i) - \frac{1}{2}E(\text{H}_2) \quad (36)$$

where we have omitted the Miller indices for brevity. $E_{\text{slab}}(\text{Cr}_{\text{Fe}}^i \text{H})$ is the energy of the slab system containing a Cr substitution in either the surface ($i=SL$) or subsurface layer ($i=SSL$), with a hydrogen in either hollow or bridge sites. $E_{\text{slab}}(\text{Cr}_{\text{Fe}}^i)$ is the same slab without the adatom. The adsorption and binding energies are presented in Table XII. The bridge site is a minimum for all considered Cr substitutions. On the other hand, sites 1 and 6 both have a negative eigenvalue indicating they are transition states. We also checked all on-top sites but found they remain to be high order saddle points (non-degenerate negative eigenvalues) and therefore not sites for adsorption.

For hydrogen in the hollow site, with Cr in either site 1 (in the subsurface layer) or site 6 (in the surface layer), we note that the hydrogen remains in the center of the hollow site. With the exception of Cr in subsurface site 3, the other Cr positions displace the hydrogen along the $\langle 110 \rangle$ direction relative to the surface normal. When Cr is in the subsurface site labelled 4 the hydrogen is pushed towards the $\langle 100 \rangle$ direction towards the quasi-threefold. It stands that even dilute impurities break symmetry and may account for quasi-threefold site detection in EELS near hydrogen saturation[152].

Just as determined by Gupta, when surface layer Cr

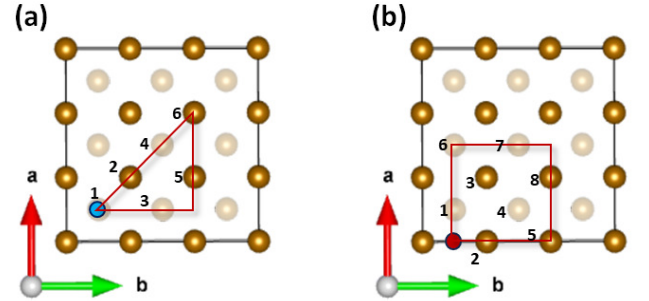


FIG. 11. Schematic of Cr surface and subsurface sites relative to a hydrogen adatom bound to (a) hollow and (b) bridge sites on a (001) $p(3 \times 3)$ Fe surface. Subsurface sites are semi-transparent.

and hydrogen in a hollow site are nearest neighbours (site 2), we find the adsorption energy to become more exothermic, from -0.378 eV in the absence of Cr to -0.388 eV. However, once a zero point energy correction is included, the relative adsorption energy for protium is reduced from -0.421 eV to -0.409 eV. When the ZPE is considered, the most exothermic arrangement for hydrogen in a hollow site is when Cr is in the subsurface site labelled 3. In this position it is the subsurface site in the adjacent unit cell. As when substituted into the bulk, the Cr atom is oversized causing the surface iron atoms between the subsurface Cr and the hydrogen in the hollow site to be pushed apart (3.10\AA or $1.09a_0$). This results

TABLE XI. Adsorption (in eV, Eqn. 33) and binding (in eV, Eqn. 34) energies of hydrogen isotope adatoms on a clean (100) terminated surface of bcc iron. An orthogonal unit cell is used to create surface covering fractions Θ (hydrogen per surface metal atom) of 0.1, 0.25 and 0.11. Daggered IDs indicate configurations which have negative eigenvalues in the vibrational analysis and therefore are not true minima.

	Absorption Energy (eV)				
	H(no ZPE) DFT	H(no ZPE) DFT	¹ H DFT	² H DFT	³ H DFT
$\Theta = 0.11, p(3 \times 3)$					
Hollow	-0.378	-0.38 ^a	-0.421	-0.408	-0.402
Quasi threefold	-0.386		-0.389	-0.388	-0.388
Bridge	-0.381	-0.34 ^a	-0.359	-0.365	-0.368
Top	0.138	0.20 ^a	0.102	0.113	0.117
$\Theta = 0.25, p(2 \times 2)$					
Hollow	-0.411	-0.38 ^a , -0.35 ^b , -0.405 ^c , -0.33 ^d	-0.444, -0.319 ^d	-0.434, -0.322 ^d	-0.430, -0.326 ^d
Quasi threefold					
Bridge	-0.385	-0.34 ^a , -0.36 ^b , -0.38 ^c , -0.27 ^d	-0.360, -0.256 ^d	-0.367, -0.26 ^d	-0.370, -0.265 ^d
Top	0.338	0.23 ^a , 0.17 ^b , 0.29 ^d	0.326, 0.250 ^d	0.326, 0.263 ^d	0.326, 0.265 ^d
$\Theta = 1, p(1 \times 1)$					
Hollow	-0.400	-0.40 ^a , -0.414 ^c	-0.426	-0.418	-0.415
Quasi threefold	-0.263		-0.263	-0.263	-0.263
Bridge	-0.276	-0.24 ^a	-0.269	-0.271	-0.272
Top	0.437	0.45 ^a	0.406	0.415	0.420
Binding Energy (eV)					
	H(no ZPE)		¹ H	² H	³ H
	DFT	DFT	DFT(IP)[Exp]	DFT	DFT
$\Theta = 0.11$					
Hollow	0.584	0.729	0.775 ^e , (0.627 ^f , 0.700 ^g), [0.82 ^h]	0.684	0.666
Quasi threefold	0.593	0.697	0.768 ^e , (0.628 ^f , 0.727 ^g)	0.665	0.651
Bridge	0.588	0.667	0.655 ^e , (0.624 ^f , 0.665 ^g)	0.642	0.631

^a Ref. 11

^b Ref. 145

^c Ref. 150

^d Ref. 22

^e Ref. 89

^f EAM potential in Ref. 151

^g EAM 'Potential A' from Ref. 89

^h Ref. 149

in the binding energy being extremely exothermic for all hydrogen isotopes. The same expansion of the hollow containing the hydrogen is also found for subsurface site 4, which has a similarly exothermic adsorption.

Surprisingly, we find that the strongest binding occurs for hydrogen in a bridge site with Cr in the subsurface (site 4). The adsorption energy for protium is -0.645 eV, approximately 50% more exothermic than any other configurations considered. As with hydrogen in the hollow site, subsurface Cr pushes neighbouring surface iron atoms apart resulting in a wider bridge for the hydrogen to be adsorbed. Whilst the most bound configurations have Cr in the subsurface layer, the segregation energy indicates that Cr has a preference to migrate to the surface layer. As such, we would expect hydrogen in the hollow first nearest neighbour to Cr on the surface

to be the more prevalent site. However, in extreme environments such as fusion reactors where neutron irradiation will exceed 50 dpa/year, the likelihood of Cr being displaced into subsurface layers is high enabling these high adsorption sites to be feasible.

E. Dipole Tensors and Relaxation Volumes

Relaxation volumes (Eqn. 6) have proven to be a remarkably universal descriptor of point [42, 76, 81, 82] and extended defects [3, 72, 78–80, 154]. Relaxation volumes are derived in this work from the elastic dipole (P_{ij}) of the relaxed configurations as outlined in Sec. II. Recent work has shown how the stress field of defects can be used to derive a body force in terms of the density of relaxation

TABLE XII. Adsorption and binding energies (in eV) of hydrogen isotope adatoms on a (100) p(3 × 3) surface with a Cr substitution in the surface (SL) or first subsurface (SSL) layer. Values in bold highlight the configurations with the strongest binding energy. Daggered IDs indicate configurations which have negative eigenvalues in the vibrational analysis and therefore are not true minima.

Cr site	ZPE	Adsorption energy				Binding energy			
		H	¹ H	² H	³ H	H	¹ H	² H	³ H
Hollow/Quasi-threefold									
1-SSL [†]	0.074	-0.340	-0.402	-0.384	-0.376	0.545	0.708	0.660	0.639
2-SL	0.117	-0.388	-0.409	-0.403	-0.401	0.594	0.715	0.680	0.664
3-SSL	0.121	-0.441	-0.458	-0.453	-0.451	0.647	0.763	0.729	0.714
4-SSL	0.160	-0.430	-0.408	-0.415	-0.417	0.636	0.714	0.691	0.681
5-SL	0.123	-0.370	-0.384	-0.380	-0.378	0.575	0.690	0.656	0.641
6-SL [†]	0.077	-0.371	-0.432	-0.414	-0.406	0.576	0.738	0.690	0.669
Bridge									
1-SSL	0.164	-0.462	-0.435	-0.443	-0.447	0.667	0.741	0.719	0.710
2-SL	0.152	-0.258	-0.243	-0.248	-0.250	0.463	0.549	0.524	0.513
3-SL	0.162	-0.340	-0.315	-0.322	-0.325	0.545	0.621	0.599	0.589
4-SSL	0.160	-0.667	-0.645	-0.651	-0.654	0.872	0.951	0.928	0.918
5-SL	0.161	-0.313	-0.290	-0.297	-0.300	0.518	0.596	0.573	0.563
6-SSL	0.161	-0.397	-0.374	-0.381	-0.384	0.602	0.680	0.657	0.647
7-SSL									
8-SL	0.161	-0.333	-0.309	-0.316	-0.320	0.539	0.615	0.593	0.583

volumes[3]. This directly enables microscopic effects of dislocations and vacancy clusters, comprised of individual point defects, to be tractably included in continuum scale dynamics[155]. Nonetheless, despite the dipole tensor being a by-product of most *ab initio* or molecular dynamics simulation, neither it or the relaxation volume are frequently reported. As a result we present elements of the dipole tensors in Table XIII and relaxation volume tensors in Table XIV, for hydrogen in different conditions within α -Fe.

Relaxation volumes are very difficult to measure and experimental studies often report a wide variability in values[156]. Interatomic potentials often poorly reproduce the relaxation volume predicted from DFT calculations[123]. Even in *ab initio* models, relaxation volumes and dipole tensors are delicately susceptible to parameters and system size. As an example of variability, the P_{11} component of a $\langle 111 \rangle$ dumbbell in tungsten varies almost 1 eV changing from a $4 \times 4 \times 4$ to $5 \times 5 \times 5$ simulation box using the same DFT *ceteris paribus* [73]. The same authors showed that for bcc vanadium, the difference in relaxation volume between a 129 atom cell and a 161 atom cell was 4.35 eV[73]. Calculations have shown full convergence of relaxation volumes requires large simulation cells which typically exceed the dimensions accessible to metallic systems in DFT calculations by approximately an order of 2. Nonetheless, dipole tensors from DFT are approximated to be within 5% accuracy and sufficient for application in continuum models[73]. Our simulation parameters, similar to Ref. 42 show good agreement with their dipole and relaxation volume tensors for a mono-vacancy.

Our calculations show that the presence of hydrogen

always exerts a positive pressure which would lead to swelling of the simulation cell. Even in a vacancy, a single trapped hydrogen halves the negative relaxation volume caused by the vacancy itself. Hydrogen pairs which arrange to produce larger (order 0.1 eV) shear components of the dipole tensor are typically repulsive. Due to the reasonably small size of our DFT simulation cells ($5 \times 5 \times 5$) it is unsurprising there is a difference in the relaxation volume with respect to a full cell relaxation. Nonetheless, allowing the cell volume to change retains the trends and behaviours just increasing the magnitude of the relaxation volume.

To contrast the relaxation volume of hydrogen with helium, another species of interest in DT fusion, we find the relaxation volume of a Helium interstitial to be $0.80\Omega_0$ and $0.83\Omega_0$ in the tetrahedral and octahedral sites, respectively. That is, the aggregated elastic size of the He interstitial and its neighbouring atoms is double that of hydrogen. Since both have outer 1s electrons one may expect their relaxation volumes to be comparable. However, recent work has shown atomic volume to be a poor predictor of relaxation volumes, particularly in α -Fe where magneto-volume effects are substantial**.

IV. CONCLUSIONS

In this work we performed zero-point energy corrected density functional theory calculations to provide fundamental insights and assess relative stabilities of different hydrogen isotopes in α -Fe and dilute FeCr. We determine that despite the diffusivity reducing for deuterium and tritium relative to protium, all hydrogen isotopes

TABLE XIII. *Ab initio* dipole tensor components P_{ij} (eV) for hydrogen (without ZPE correction) in α -Fe. The ID corresponds to configurations in Tables V and VI. $H_{T \rightarrow T}$ is the transition state of the minimum energy path between two tetrahedral sites.

ID	P_{11}	P_{22}	P_{33}	P_{12}	P_{23}	P_{31}
Hydrogen in interstitial sites:						
H_{TET}	5.230	5.230	4.700	0.000	0.000	0.000
	4.33 ^a , 4.77 ^b	4.33 ^a , 4.77 ^b	3.67 ^a , 4.20 ^b			
H_{OCT}	3.561	3.561	8.007	0.000	0.000	0.000
	3.48 ^b	3.48 ^b	8.17 ^b			
$H_{T \rightarrow T}$	4.137	4.137	7.014	0.737	0.000	0.000
Two hydrogen in tetrahedral interstitial sites:						
2H2	13.004	9.020	8.142	0.000	0.000	0.000
2H3	11.384	9.338	9.336	-0.241	-0.116	-0.247
2H4	10.335	9.333	10.335	0.053	-0.053	-0.027
2H5	10.557	9.812	9.863	0.000	-0.002	0.000
2H6	10.430	9.345	10.440	-0.106	-0.107	-0.145
2H7	10.714	9.741	9.946	0.164	-0.053	0.135
2H8a	10.385	9.307	10.385	0.000	0.000	0.000
2H8b	11.203	9.817	9.475	0.000	-0.004	0.000
2H9a	10.372	9.941	10.367	0.082	-0.078	0.101
2H9b	11.039	9.824	9.826	0.000	-0.253	0.000
2H10a	10.549	10.238	9.403	0.000	-0.036	0.000
2H10b	11.424	9.974	9.426	0.000	-0.222	0.000
2H11	9.869	10.534	9.852	-0.025	-0.023	-0.057
2H12	10.397	10.480	9.313	-0.014	-0.033	-0.046
0-7 hydrogen trapped in mono-vacancy:						
1V	-2.929	-2.929	-2.929	0.000	0.000	0.000
	-3.081 ^c	-3.081 ^c	-3.081 ^c	0.000 ^c	0.000 ^c	0.000 ^c
	-3.682 ^d	-3.682 ^d	-3.682 ^d	0.000 ^d	0.000 ^d	0.000 ^d
1V1H	-1.573	-1.573	-1.573	0.000	0.000	0.000
1V2H	0.422	0.422	0.982	0.000	0.000	0.000
1V2Hb	0.507	0.966	0.966	0.000	0.217	0.000
1V3H	2.772	4.015	3.362	0.000	0.000	0.000
1V3Hb	3.542	3.542	3.542	0.158	-0.158	-0.158
1V4H	4.501	7.363	7.363	0.000	0.000	0.000
1V4Hb	6.340	6.340	6.340	1.195	0.000	0.000
1V5H	9.349	9.923	9.923	0.000	0.000	0.000
1V6H	12.611	12.611	12.611	0.000	0.000	0.000
1V6Hb	12.590	12.590	12.590	0.000	0.000	0.000
1V7H						
Hydrogen decorating a self interstitial atom						
$\langle 110 \rangle$	26.047	22.196	22.196	0.000	4.607	0.000
	25.832 ^c	21.143 ^c	21.143 ^c 0.000 ^c	5.122 ^c	0.000 ^c	
	24.853 ^d	20.534 ^d	20.534 ^d	0.000 ^d	4.620 ^d	0.000 ^d
$\langle 110 \rangle H1$			Relaxed to configuration $\langle 110 \rangle_{DB} H4$			
$\langle 110 \rangle H2$	30.452	27.466	26.848	0.115	4.830	-0.186
$\langle 110 \rangle H3$	30.325	27.381	26.132	0.384	4.775	-0.508
$\langle 110 \rangle H4$	30.325	27.381	26.132	0.384	4.775	-0.508
$\langle 110 \rangle H5$			Configuration unstable. H ejected.			
$\langle 110 \rangle H6$	29.585	26.881	27.425	0.002	5.488	0.004
$\langle 110 \rangle H7$	31.373	27.153	25.894	-0.002	4.521	-0.002
$\langle 110 \rangle H8$	30.639	26.393	27.414	0.005	4.524	-0.001

^a Ref.157 extracted from Ref. 123

^b Ref.158 extracted from Ref. 123

^c Ref.42

^d Ref.76

TABLE XIV. Relaxation volume tensor components Ω_{ij} and relaxation volume $\text{Tr}(\Omega_{ij})$ for hydrogen (without ZPE correction) in α -Fe. The relaxation volume is presented both in \AA^3 and in reduced units ($\Omega_0/\Omega_0^{\text{Fe}}$), where $\Omega_0^{\text{Fe}} = a_0^3/2 = 11.36\text{\AA}^3$ is the atomic volume of iron. Relaxation volumes are calculated at fixed volume. Where calculations have been repeated with cell relaxation we also present the values in the format ‘fixed cell/relaxed cell’. ID links to configurations in Tables V and VI. $H_{T \rightarrow T}$ is the transition state of the minimum energy path between two tetrahedral sites.

ID	Ω_{11} (\AA^3)	Ω_{22} (\AA^3)	Ω_{33} (\AA^3)	Ω_{12} (\AA^3)	Ω_{23} (\AA^3)	Ω_{31} (\AA^3)	Ω_0 (\AA^3)	$\Omega_0/\Omega_0^{\text{Fe}}$	
Hydrogen in interstitial sites:									
H_{TET}	1.635/1.705	1.635/1.705	0.846/0.847	0.000/0.000	0.000/0.000	0.000/0.000	4.118/4.256	0.36(3)/0.37(5) 0.311 ^a	
H_{OCT}	-0.837/-0.853	-0.837/-0.853	5.784/5.998	0.000/0.000	0.000/0.000	0.000/0.000	4.110/4.293	0.36(2)/0.37(8) 0.300 ^a	
$H_{T \rightarrow T}$	-0.044	-0.044	4.241	0.602	0.000	0.000	4.154	0.36(6) 0.297 ^a	
Two hydrogen in tetrahedral interstitial sites:									
2H2	7.123	1.188	-0.118	0.000	0.000	0.000	8.194	0.72(1)	
2H3	4.754	1.706	1.704	-0.197	-0.095	-0.202	8.164	0.71(9)	
2H4	3.213	1.722	3.214	0.043	-0.043	-0.023	8.150	0.71(7)	
2H5	3.451	2.342	2.419	0.000	-0.002	0.000	8.212	0.72(3)	
2H6	3.269	1.653	3.285	-0.087	-0.088	-0.119	8.207	0.72(2)	
2H7	3.616	2.168	2.474	0.134	-0.043	0.110	8.258	0.72(7)	
2H8a	3.258	1.653	3.259	0.000	0.000	0.000	8.170	0.71(9)	
2H8b	4.307	2.243	1.734	0.000	-0.004	0.000	8.283	0.72(9)	
2H9a	2.994	2.353	2.987	0.067	-0.064	0.082	8.334	0.73(4)	
2H9b	3.984	2.174	2.178	0.000	-0.207	0.000	8.336	0.73(4)	
2H10a	3.456	2.994	1.751	0.000	0.029	0.000	8.201	0.72(2)	
2H10b	4.502	2.343	1.527	0.000	-0.182	0.000	8.373	0.73(7)	
2H11	2.417	3.409	2.393	-0.024	-0.019	-0.047	8.219	0.72(3)	
2H12	3.230	3.354	1.616	-0.012	-0.027	-0.038	8.201	0.72(2)	
0-7 hydrogen trapped in mono-vacancy:									
1V	-0.795/-0.843 -0.831 ^b -1.015 ^c	-0.795/-0.843 -0.831 ^b -1.015 ^c	-0.795/-0.843 -0.831 ^b -1.015 ^c	0.000/0.000 0.000 ^b 0.000 ^c	0.000/0.000 0.000 ^b 0.000 ^c	0.000/0.000 0.000 ^b 0.000 ^c	0.000/0.000 0.000 ^b 0.000 ^c	-2.387/-2.529 -3.045 ^c	-0.21(0)/-0.22(3) -0.22 ^b
1V1H	-0.550/-0.584	-0.550/-0.584	-0.100/-0.113	0.000/0.000	0.000/0.000	0.000/0.000	-1.200/-1.281	-0.10(6)/-0.11(3)	
1V2H	-0.113/-0.149	-0.113/-0.149	0.721/0.809	0.000/0.000	0.000/0.000	0.000/0.000	0.496/0.511	0.04(4)/0.04(5)	
1V2Hb	-0.236/-0.286	0.449/0.501	0.449/0.501	0.000/0.000	0.178/0.200	0.000/0.000	0.663/0.714	0.05(8)/0.06(3)	
1V3H	0.008/-0.019	1.860/1.951	0.889/0.969	0.000/0.000	0.000/0.000	0.000/0.000	2.757/2.900	0.24(3)/0.255	
1V3Hb	0.962/0.993	0.962/0.993	0.962/0.993	0.129/0.133	-0.129/-0.133	-0.129/-0.133	2.887/2.979	0.25(4)/0.26(2)	
1V4H	-1.102/-1.149	3.163/3.286	3.162/3.286	0.000/0.000	0.000/0.000	0.000/0.000	5.222/5.424	0.46(0)/0.47(0)	
1V4Hb	1.649/1.715	1.650/1.715	1.916/2.005	0.977/0.9643	0.000/0.000	0.000/0.000	5.215/5.435	0.45(9)/0.47(8)	
1V5H	2.073/2.166	2.929/3.039	2.929/3.039	0.000/0.000	0.000/0.000	0.000/0.000	7.930/8.245	0.69(8)/0.72(6)	
1V6H	3.425	3.426	3.426	0.000	0.000	0.000	10.277	0.90(5)	
1V6Hb	3.278/3.440	3.279/3.440	3.798/3.440	0.000/0.000	0.000/0.000	0.000/0.000	10.354/10.802	0.91(1)/0.95(1)	
1V7H	4.512/4.738	4.512/4.738	4.512/4.738	0.000/0.000	0.000/0.000	0.000/0.000	13.540/14.213	1.19(2)/1.25(1)	
Hydrogen decorating a self interstitial atom									
$\langle 110 \rangle_{DB}$	10.201	4.466	4.466	0.000	3.764	0.000	19.133		
	9.777	4.294	4.302	0.000	3.819	0.000			
	6.851	5.660	5.660	0.000	1.274	0.000	18.171		
$\langle 110 \rangle_{DBH1}$				Relaxed to config $\langle 110 \rangle_{H4}$					
$\langle 110 \rangle_{DBH2}$	10.945	6.500	5.580	0.094	3.946	-0.153	23.025		
$\langle 110 \rangle_{DBH3}$									
$\langle 110 \rangle_{DBH4}$	11.224	6.656	4.899	0.302	3.894	-0.414	22.779		
$\langle 110 \rangle_{DBH5}$				Unstable configuration.					
$\langle 110 \rangle_{DBH6}$	10.008	5.984	6.795	0.002	4.484	0.002	22.788		
$\langle 110 \rangle_{DBH7}$	12.458	6.174	4.300	-0.001	3.694	-0.002	22.931		
$\langle 110 \rangle_{DBH8}$	11.354	5.031	6.554	0.004	3.696	-0.002	22.938		

^a Ref. 159 using interatomic potential.

^b Ref.42 using DFT.

^c Ref.76 using DFT.

are highly mobile within bcc iron. All isotopes reside in tetrahedral interstitial sites. Protium migrates via the octahedral site whilst tritium takes a rotational pathway to the adjacent tetrahedral site. Energy barriers for both pathways are degenerate for deuterium allowing it to become the most mobile isotope at fusion operating conditions. Cr solutes repel hydrogen and increase the effective migration barriers via the octahedral site by up to 20 meV for each isotope. Binding energies between Cr and tritium are particularly repulsive and remain so for distances over multiple lattice parameters.

Hydrogen trapping in a mono-vacancy compares extremely favorably to previous calculations[12, 132], with binding energies for deuterium closely matching desorption stages of ion-beam implantation-annealing experiments[1, 2]. Hydrogen prefers to reside in near octahedral sites on the vacancy faces with attractive binding energies for up to six hydrogen. The binding energy is exothermic for four trapped protium, or 5 deuterium/tritium isotopes. In these highly saturated vacancy complexes the formation energy is negative and may explain the absence of hydride phases at low hydrogen pressure. Cr neighbouring a monovacancy increases the available volume within the vacant site making a single trapped hydrogen the most bound configuration. Nonetheless, our calculations predict the complex cannot trap more hydrogen than a mono-vacancy. Cr causes hydrogen to be displaced from the near octahedral sites. The relative position of hydrogen in the vacancy affects the magnetic moment of Cr substitution.

We find the (110) surface to be most stable with a surface energy of 2.41 Jm^2 which matches liquid tension experiments[143]. All hydrogen isotopes have strong exothermic binding to both (100) and (110) surfaces. On the 110 surface at low surface coverage a quasi-threefold

site has the highest adsorption energy for all hydrogen isotopes. In the $p(2 \times 1)$ phase the symmetric stretch mode of protium closely agrees with electron energy loss spectroscopy [148]. The binding energy is reduced for deuterium and tritium. On the (100) surface we predict the hollow site to be the strongest adsorption site at all coverages. The relative difference in binding energy between the different isotopes is only 10-15 meV so we do not expect appreciable kinetic isotope effects for surface adsorption. When a Cr substitution is made the energy of segregation shows it prefers to reside on the surface layer. However, subsurface Cr is found to increase the length of the surrounding surface bridge sites increasing the adsorption energy up to 50% making it more stable than the hollow or quasi-threefold site on a (100) surface.

Finally, we presented the elastic dipole tensors and relaxation volumes of the Fe-H configurations which can be used to represent source terms in continuum models of irradiated materials.

ACKNOWLEDGMENTS

This work has been carried out within the framework of the EUROfusion Consortium and has received funding from the Euratom research and training programme 2014-2018 and 2019-2020 under grant agreement No 633053. The views and opinions expressed herein do not necessarily reflect those of the European Commission. This work also received funding from the Euratom research and training programme 2019-2020 under grant agreement No. 755039. We acknowledge funding by the RCUK Energy Programme (Grant No. EP/T012250/1), and EUROfusion for providing access to Marconi-Fusion HPC facility in the generation of data used in this manuscript.

-
- [1] F. Besenbacher, S. Myers, P. Nordlander, and J. Nørskov, *Journal of Applied Physics* **61**, 1788 (1987).
- [2] S. Myers, D. Follstaedt, F. Besenbacher, and J. Böttiger, *Journal of Applied Physics* **53**, 8734 (1982).
- [3] S. L. Dudarev, D. R. Mason, E. Tarleton, P.-W. Ma, and A. E. Sand, *A multi-scale model for stresses, strains and swelling of reactor components under irradiation*, *Nuclear Fusion* **58**, 126002 (2018).
- [4] J. P. Hirth, *Metallic Transactions A* **11**, 861 (1980).
- [5] A. Oriani, *Hydrogen embrittlement of steels*, *Annual Review in Materials Science* **8**, 327 (1978).
- [6] S. M. Myers, M. I. Baskes, H. K. Birnbaum, J. W. Corbett, G. G. DeLeo, S. K. Estreicher, E. E. Haller, P. Jena, N. M. Johnson, R. Kirchheim, S. J. Pearton, and M. J. Stavola, *Reviews of Modern Physics* **64**, 559 (1992).
- [7] D. Hardie, E. A. Charles, and A. H. Lopez, *Hydrogen embrittlement of high strength pipeline steels*, *Corrosion Science* **48**, 4378 (2006).
- [8] W. H. Johnson, *Nature* **11**, 393 (1875).
- [9] F. A. Nichols, *Hydrogen degradation of ferrous alloys*, edited by richard a. oriani, john p. hirth, and michael smialowski (1985, noyes publications), *MRS Bulletin* **11**, 3–3 (1986).
- [10] J. Song and W. A. Curtin, *Atomic mechanism and prediction of hydrogen embrittlement in iron*, *Nature Materials* **12**, 145 (2012).
- [11] D. E. Jiang and E. A. Carter, *Diffusion of interstitial hydrogen into and through bcc fe from first principles*, *Physical Review B* **70**, 064102 (2004).
- [12] E. Hayward and C.-C. Fu, *Interplay between hydrogen and vacancies in α -fe*, *Physical Review B* **87**, 174103 (2013).
- [13] D. R. Mason, D. Nguyen-Manh, V. W. Lindblad, F. G. Granberg, and M.-Y. Lavrentiev, *An empirical potential for simulating hydrogen isotope retention in highly irradiated tungsten*, *Journal of Physics: Condensed Matter* **35**, 95901 (2023).
- [14] A. J. Samin, D. A. Andersson, E. F. Holby, and B. P. Uberuaga, *First-principles localized cluster expansion study of the kinetics of hydrogen diffusion in homogeneous and heterogeneous fe-cr alloys*, *Physical Review*

- B **99**, 014110 (2019).
- [15] F.-S. Meng, J.-P. Du, S. Shinzato, H. Mori, P. Yu, K. Matsubara, N. Ishikawa, and S. Ogata, General-purpose neural network interatomic potential for the α -iron and hydrogen binary system: Toward atomic-scale understanding of hydrogen embrittlement, *Physical Review Materials* **5**, 113606 (2021).
- [16] D. Stork, P. Agostini, J.-L. Boutard, D. Buckthorpe, E. Diegele, S. Dudarev, C. English, G. Federici, M. R. Gilbert, S. Gonzalez, A. Ibarra, C. Linsmeier, A. L. Puma, G. Marbach, L. W. Packer, B. Raj, M. Rieth, M. Q. Tran, D. J. Ward, and S. J. Zinkle, Materials rd for a timely demo: Key findings and recommendations of the eu roadmap materials assessment group, *Fusion Engineering and Design* **89**, 1586 (2014).
- [17] L. Malerba, M. Caturla, E. Gaganidze, C. Kaden, M. Konstantinović, P. Olsson, C. Robertson, D. Rodney, A. Ruiz-Moreno, M. Serrano, J. Aktaa, N. Anento, S. Austin, A. Bakaev, J. Balbuena, F. Bergner, F. Boioli, M. Boleininger, G. Bonny, N. Castin, J. Chapman, P. Chekhonin, M. Clozel, B. Devincere, L. Dupuy, G. Diego, S. Dudarev, C.-C. Fu, R. Gatti, L. Gélébart, B. Gómez-Ferrer, D. Gonçalves, C. Guerrero, P. Gueye, P. Hähner, S. Hannula, Q. Hayat, M. Hernández-Mayoral, J. Jagielski, N. Jennett, F. Jiménez, G. Kapoor, A. Kraych, T. Khvan, L. Kurpaska, A. Kuronen, N. Kvashin, O. Libera, P.-W. Ma, T. Manninen, M.-C. Marinica, S. Merino, E. Meslin, F. Momprou, F. Mota, H. Namburi, C. Ortiz, C. Pareige, M. Prester, R. Rajakrishnan, M. Sauzay, A. Serra, I. Simonovski, F. Soisson, P. Spätig, D. Tanguy, D. Terentyev, M. Trebala, M. Trochet, A. Ulbricht, M. Vallet, K. Vogel, T. Yalcinkaya, and J. Zhao, Multi-scale modelling for fusion and fission materials: The m4f project, *Nuclear Materials and Energy* **29**, 101051 (2021).
- [18] UKAEA, Uk fusion materials roadmap 2021-2040 (2021).
- [19] IEA, Iron and steel technology roadmap – analysis (2020).
- [20] T. Battle, U. Srivastava, J. Kopfle, R. Hunter, and J. McClelland, Chapter 1.2 - the direct reduction of iron, in *Treatise on Process Metallurgy*, edited by S. Seetharaman (Elsevier, Boston, 2014) pp. 89–176.
- [21] D. E. Jiang and E. A. Carter, Adsorption and diffusion energetics of hydrogen atoms on fe(110) from first principles, *Surface Science* **547**, 85 (2003).
- [22] A. Boda, S. M. Ali, K. T. Shenoy, and S. Mohan, Adsorption, absorption, diffusion, and permeation of hydrogen and its isotopes in bcc bulk fe and fe(100) surface: Plane wave-based density functional theoretical investigations, *Journal of Physical Chemistry C* **123**, 23951 (2019).
- [23] S. Taketomi, R. Matsumoto, and N. Miyazaki, Atomistic study of hydrogen distribution and diffusion around a {112}<111> edge dislocation in alpha iron, *Acta Materialia* **56**, 3761 (2008).
- [24] S. Wang, K. Takahashi, N. Hashimoto, S. Isobe, and S. Ohnuki, Strain field of interstitial hydrogen atom in body-centered cubic iron and its effect on hydrogen–dislocation interaction, *Scripta Materialia* **68**, 249 (2013).
- [25] B. Irigoyen, R. Ferullo, N. Castellani, and A. Juan, The location of a hydrogen atom and hydrogen molecules in bcc fe: an ased-mo approach, *Modelling and Simulation in Materials Science and Engineering* **3**, 319 (2002).
- [26] E. Hayward, B. Beeler, and C. Deo, *Philosophical Magazine Letters* **92**, 217 (2012).
- [27] E. Hayward and C. Deo, Energetics of small hydrogen–vacancy clusters in bcc iron, *Journal of Physics: Condensed Matter* **23**, 425402 (2011).
- [28] Y. Teteyama and T. Ohno, Stability and clusterization of hydrogen-vacancy complexes in α -fe: An ab initio study, *Physical Review B* **67**, 174105 (2003).
- [29] W. T. Geng, J. P. Du, A. Ishii, N. Ishikawa, H. Kimizuka, and K. Ogata, *Scripta Materialia* **134**, 105 (2017).
- [30] C. W. Waggoner, A relation between the magnetic and elastic properties of a series of unhardened iron-carbon alloys, *Phys. Rev. (Series I)* **35**, 58 (1912).
- [31] K. Mergia and N. Boukos, Structural, thermal, electrical and magnetic properties of Eurofer 97 steel, *Journal of Nuclear Materials* **373**, 1 (2008).
- [32] H. Hasegawa, M. W. Finnis, and D. G. Pettifor, A calculation of elastic constants of ferromagnetic iron at finite temperatures, *Journal of Physics F: Metal Physics* **15**, 19 (1985).
- [33] D. J. Dever, Temperature dependence of the elastic constants in α -iron single crystals: relationship to spin order and diffusion anomalies, *Journal of Applied Physics* **43**, 3293 (1972).
- [34] V. I. Razumovskiy, A. V. Ruban, and P. A. Korzhavyi, Effect of temperature on the elastic anisotropy of pure Fe and Fe_{0.9}Cr_{0.1} random alloy, *Physical Review Letters* **107**, 205504 (2011).
- [35] H. Hasegawa and D. G. Pettifor, Microscopic theory of the temperature-pressure phase diagram of iron, *Physical Review Letters* **50**, 130 (1983).
- [36] F. Körmann, A. Dick, B. Grabowski, B. Hallstedt, T. Hickel, and J. Neugebauer, Free energy of bcc iron: Integrated ab initio derivation of vibrational, electronic, and magnetic contributions, *Physical Review B* **78**, 033102 (2008).
- [37] M. Y. Lavrentiev, D. Nguyen-Manh, and S. L. Dudarev, Magnetic cluster expansion model for bcc-fcc transitions in Fe and Fe-Cr alloys, *Physical Review B* **81**, 184202 (2010).
- [38] M. Y. Lavrentiev, R. Soulaïrol, C. C. Fu, D. Nguyen-Manh, and S. L. Dudarev, Noncollinear magnetism at interfaces in iron-chromium alloys: The ground states and finite-temperature configurations, *Physical Review B* **84**, 144203 (2011).
- [39] F. Körmann, T. Hickel, and J. Neugebauer, Influence of magnetic excitations on the phase stability of metals and steels, *Current Opinion in Solid State and Materials Science* **20**, 77 (2016).
- [40] P.-W. Ma, S. L. Dudarev, and J. S. Wrobel, Dynamic simulation of structural phase transitions in magnetic iron, *Physical Review B* **96**, 094418 (2017).
- [41] D. Nguyen-Manh, A. P. Horsfield, and S. L. Dudarev, Self-interstitial atom defects in bcc transition metals: Group-specific trends, *Physical Review B* **73**, 020101(R) (2006).
- [42] P.-W. Ma and S. L. Dudarev, Universality of point defect structure in body-centered cubic metals, *Physical Review Materials* **3**, 013605 (2019).
- [43] J. B. J. Chapman, P. W. Ma, and S. L. Dudarev, Effect of non-heisenberg magnetic interactions on defects

- in ferromagnetic iron, *Physical Review B* **102**, 224106 (2020).
- [44] M. Mrovec, D. Nguyen-Manh, C. Elsässer, and P. Gumbsch, Magnetic bond-order potential for iron, *Physical Review Letters* **106**, 246402 (2011).
- [45] J. B. J. Chapman and P.-W. Ma, A machine-learned spin-lattice potential for dynamic simulations of defective magnetic iron, *Scientific Reports* **12**, 22451 (2022).
- [46] D. Nguyen-Manh, M. Y. Lavrentiev, and S. L. Dudarev, Magnetic origin of nano-clustering and point defect interaction in fe-cr alloys: an ab-initio study, *J. Computer-Aided Mater. Des.* **14**, 159 (2007).
- [47] J. B. J. Chapman, P.-W. Ma, and S. L. Dudarev, Dynamics of magnetism in fe-cr alloys with cr clustering, *Physical Review B* **99**, 184413 (2019).
- [48] H. Grabke and E. Rieche, Absorption and diffusion of hydrogen in steels, *Materiali in tehnologije* **34**, 331 (2000).
- [49] M. Nagumo, M. Nakamura, and K. Takai, *Metallic Materials Transactions A* **32A**, 339 (2001).
- [50] R. Iyer and H. Pickering, *Annual Reviews in Material Science* **20**, 299 (1990).
- [51] Y. Fukai and N. Okuma, *Japanese Journal of Applied Physics* **32**, L1256 (1993).
- [52] M. Iwamoto and Y. Fukai, *Material Transactions JIM* **40**, 606 (1999).
- [53] V. Antonov, Neutron diffraction investigation of the dhcp and hcp iron hydrides and deuterides, *Journal of Alloys and Compounds* **264**, 214 (1998).
- [54] V. Antonov, I. Belash, V. Degtyareva, E. Ponyatovskii, and V. Shiryayev, Obtaining iron hydride under high hydrogen pressure, *Soviet Physics Doklady* **25**, 490 (1980).
- [55] Y. Fukai, Formation of superabundant vacancies in m-h alloys and some of its consequences: a review, *Journal of Alloys and Compounds* **263**, 356 (2003).
- [56] H. Birnbaum and P. Sofronis, *Materials Science and Engineering A* **176**, 191 (1994).
- [57] R. Oriani and P. Josephic, *Acta Metallica* **25**, 979 (1977).
- [58] P. Nordlander, J. K. Nørskov, F. Besenbacher, and S. M. Myers, Multiple deuterium occupancy of vacancies in pd and related metals, *Physical Review B* **40**, 1990(R) (1989).
- [59] J. Shi and N. Hashimoto, Study on synergistic effects of h and he in -fe, *Nuclear Materials and Energy* **16**, 212 (2018).
- [60] I. A. E. Agency, *Management of Waste Containing Tritium and Carbon-14*, Technical Reports Series - International Atomic Energy Agency (International Atomic Energy Agency, 2004).
- [61] G. Kresse and J. Hafner, Ab initio molecular dynamics for liquid metals, *Physical Review B* **47**, 558(R) (1993).
- [62] G. Kresse and J. Hafner, Ab initio molecular-dynamics simulation of the liquid-metal-amorphous-semiconductor transition in germanium, *Physical Review B* **49**, 14251 (1994).
- [63] G. Kresse and J. Furthmüller, Efficiency of ab initio total energy calculations for metals and semiconductors using a plane-wave basis set, *Computational Materials Science* **6**, 15 (1996).
- [64] G. Kresse and J. Furthmüller, Efficient iterative schemes for ab initio total-energy calculations using a plane-wave basis set, *Physical Review B* **54**, 11169 (1996).
- [65] P. E. Blöchl, Projector augmented-wave method, *Physical Review B* **50**, 17953 (1994).
- [66] G. Kresse and D. Joubert, From ultrasoft pseudopotentials to the projector augmented-wave method, *Physical Review B* **59**, 1758 (1999).
- [67] J. P. Perdew, K. Burke, and M. Ernzerhof, Generalized gradient approximation made simple, *Physical Review Letters* **77**, 3865 (1996).
- [68] J. P. Perdew, K. Burke, and M. Ernzerhof, Erratum: Generalized gradient approximation made simple, *Physical Review Letters* **78**, 1396 (1997).
- [69] H.J.Monkhorst and J.D.Pack, Special points for Brillouin-zone integrations, *Physical Review B* **13**, 5188 (1976).
- [70] M. Methfessel and A. T. Paxton, *Physical Review B* **40**, 3616 (1989).
- [71] P. Pulay, *Chemical Physics* **73**, 393 (1980).
- [72] C. Varvenne, F. Bruneval, M. C. Marinica, and E. Clouet, Point defect modeling in materials: Coupling ab initio and elasticity approaches, *Physical Review B* **88**, 134102 (2013).
- [73] S. L. Dudarev and P. W. Ma, Elastic fields, dipole tensors, and interaction between self-interstitial atom defects in bcc transition metals, *Physical Review Materials* **2**, 033602 (2018).
- [74] P. W. Ma and S. L. Dudarev, CALANIE: Anisotropic elastic correction to the total energy, to mitigate the effect of periodic boundary conditions, *Computer Physics Communication* **252**, 107130 (2020).
- [75] D. M. Barnett, The precise evaluation of derivatives of the anisotropic elastic green's functions, *Physica Status* **49**, 741 (1972).
- [76] J. S. Wróbel, M. R. Zemła, D. Nguyen-Manh, P. Olsson, L. Messina, C. Domain, T. Wejrzanowski, and S. L. Dudarev, Elastic dipole tensors and relaxation volumes of point defects in concentrated random magnetic fe-cr alloys, *Computational Materials Science* **194**, 110435 (2021).
- [77] F. Hofmann, D. Nguyen-Manh, M. R. Gilbert, C. E. Beck, J. K. Eliason, A. A. Maznev, W. Liu, D. E. J. Armstrong, K. A. Nelson, and S. L. Dudarev, Lattice swelling and modulus change in a helium-implanted tungsten alloy: X-ray micro-diffraction, surface acoustic wave measurements, and multiscale modelling, *Acta Mater.* **89**, 352 (2015).
- [78] D. Mason, D. Nguyen-Manh, and C. Becquart, An empirical potential for simulating vacancy clusters in tungsten, *Journal of Physics: Condensed Matter* **29**, 505501 (2017).
- [79] D. R. Mason, D. Nguyen-Manh, M.-C. Marinica, R. Alexander, A. E. Sand, and S. L. Dudarev, Relaxation volumes of microscopic and mesoscopic irradiation-induced defects in tungsten, *Journal of Applied Physics* **126**, 075112 (2019).
- [80] P.-W. Ma, D. R. Mason, and S. L. Dudarev, Multi-scale analysis of dislocation loops and voids in tungsten, *Physical Review Materials* **4**, 103609 (2020).
- [81] P.-W. Ma and S. L. Dudarev, Effect of stress on vacancy formation and migration in body-centered-cubic metals, *Physical Review B* **3**, 063601 (2019).
- [82] C. Varvenne, F. Bruneval, M.-C. Marinica, and E. Clouet, Point defect modeling in materials: Coupling ab initio and elasticity approaches, *Physical Review B* **88**, 134102 (2013).
- [83] S. Baroni, S. d. Gironcoli, A. D. Corso, and P. Gi-

- annozzi, Phonons and related crystal properties from density-functional perturbation theory, *Reviews of Modern Physics* **73**, 515 (2001).
- [84] S. Guha, J. Menéndez, J. B. Page, G. B. Adams, G. S. Spenser, J. P. Lehman, P. Giannozzi, and S. Baroni, *Physical Review Letters* **72**, 3359 (1994).
- [85] J. M. Zhang, T. Ruf, M. Cardona, O. Ambacher, M. Stutzmann, J.-M. Wagner, and F. Bechstedt, *Physical Review B* **56**, 14399 (1997).
- [86] L. Katz, M. Guinan, and R. Borg, Diffusion of h_2 , d_2 , and t_2 in single-crystal ni and cu, *Physical Review B* **4**, 330 (1971).
- [87] W. Kehr, in *Hydrogen in Metals I*, edited by G. Alefield and J. Völkl (Springer, Berlin, 1978) p. 197.
- [88] Y. Cui, C. Hu, P. Yu, D. Xie, L. Kong, Y. Rong, M. Wen, and J. Zou, Enhanced h-h binding and consequent hagggregation around dislocation in α -fe lattice, *Materials Research Express* **7**, 066518 (2020).
- [89] A. Ramasubramaniam, M. Itakura, and E. A. Carter, Interatomic potentials for hydrogen in α -iron based on density functional theory, *Physical Review B* **2009**, 174101 (2009).
- [90] M. Methfessel, M. v. Schilfgaarde, and M. Scheffle, *Physical Review Letters* **70**, 29 (1993).
- [91] C. J. Pickard and R. J. Needs, *Nature Physics* **3**, 473 (2007).
- [92] C. Wolverton, V. Ozolins, and M. Asta, *Physical Review B* **69**, 144109 (2004).
- [93] B. Cheng, A. T. Paxton, and M. Ceriotti, Hydrogen diffusion and trapping in α -fe - the role of quantum and anharmonic fluctuations, *Physical Review Letters* **120**, 225901 (2018).
- [94] A. T. Paxton and I. H. Katzarov, Quantum and isotope effects on hydrogen diffusion, trapping and escape in iron, *Acta Materialia* **103**, 71 (2016).
- [95] K. P. Huber and G. Herzberg, Constants of diatomic molecules, in *Molecular Spectra and Molecular Structure: IV. Constants of Diatomic Molecules* (Springer US, Boston, MA, 1979) pp. 8-689.
- [96] A. Boda, S. Bajania, S. M. Ali, K. Shenoy, and S. Mohan, Chemisorption, diffusion and permeation of hydrogen isotopes in bcc bulk cr and cr(100) surface: First-principles dft simulations, *Journal of Nuclear Materials* **543**, 152538 (2021).
- [97] Y. Bai, B. W. J. Chen, G. Peng, and M. Mavrikakis, Density functional theory study of thermodynamic and kinetic isotope effects of h_2/d_2 dissociative adsorption on transition metals, *Catalysis Science and Technology* **8**, 3321 (2018).
- [98] G. D. Dickenson, M. L. Niu, E. J. Salumbides, J. Komasa, K. S. E. Eikema, K. Pachucki, and W. Ubachs, Fundamental vibration of molecular hydrogen, *Physical Review Letters* **110**, 193601 (2013).
- [99] K. K. Irikura, Experimental vibrational zero-point energies: Diatomic molecules, *Journal of Physical and Chemical Reference Data* **38**, 749 (2009).
- [100] K. Heinola and T. Ahlgren, *Journal of Applied Physics* **107**, 113531 (2010).
- [101] A. Moitra and K. Solanki, *Computational Materials Science* **50**, 2291 (2011).
- [102] F. Johnson and E. A. Carter, *Journal of Materials Research* **25**, 315 (2011).
- [103] C. Ouyang and Y.-S. Lee, *Physical Review B* **83**, 045111 (2011).
- [104] G. Sundell and G. Wahnstrom, *Physical Review B* **70**, 224301 (2004).
- [105] Y. Hayashi and W. M. Shu, Iron (ruthenium and osmium)-hydrogen systems, *Solid State Phenomena* **73-75**, 65 (2000).
- [106] J. Murrell and K. Laidler, Symmetries of activated complexes, *Transactions of the Faraday Society* **64**, 371 (1968).
- [107] D. J. Wales and R. S. Berry, Limitations of the murrell-laidler theorem, *Journal of the Chemical Society, Faraday Transactions* **88**, 543 (1992).
- [108] Y. Fukai, *The Metal-hydrogen System: Basic Bulk Properties*, Lecture Notes in Economic and Mathematical Systems (Springer-Verlag, 1993).
- [109] H. Hagi, Diffusion coefficient of hydrogen in iron without trapping by dislocations and impurities, *Material Transactions JIM* **35**, 112 (1994).
- [110] K. Kiuchi and McLellan, The solubility and diffusivity of hydrogen in well-annealed and deformed iron, *Acta Metallurgica* **31**, 961 (1983).
- [111] A. Boda, M. A. Sk, K. Shenoy, and S. Mohan, Diffusion, permeation and solubility of hydrogen, deuterium and tritium in crystalline tungsten: First principles dft simulations, *International Journal of Hydrogen Energy* **45**, 29095 (2020).
- [112] C. Cabet, F. Dalle, E. Gaganidze, J. Henry, and H. Tanigawa, Ferritic-martensitic steels for fission and fusion applications, *Journal of Nuclear Materials* **523**, 510 (2019).
- [113] J. O. Andersson and B. Sundman, thermodynamic properties of the cr-fe system, *CALPHAD* **11**, 83 (1987).
- [114] D. Nguyen-Manh, M. Y. Lavrentiev, and S. L. Dudarev, The fe-cr system: atomistic modelling of thermodynamic and kinetics of phase transformations, *C. R. Physique* **9**, 379 (2008).
- [115] D. Nguyen-Manh, M. Y. Lavrentiev, and S. L. Dudarev, Ab initio and monte carlo modeling in fe-cr system: Magnetic origin of anomalous thermodynamic and kinetic properties, *Computational Materials Science* **44**, 1 (2008).
- [116] D. Nguyen-Manh and S. L. Dudarev, Model many-body Stoner Hamiltonian for binary FeCr alloys, *Physical Review B* **80**, 104440 (2009).
- [117] W. Xiong, M. Selleby, Q. Chen, J. Odqvist, and Y. Du, Phase equilibria and thermodynamic properties in the fe-cr system, *Critical Reviews in Solid State and Materials Science* **35**, 125 (2010).
- [118] G. Bonny, D. Terentyev, and L. Malerba, On the α - α miscibility gap of fe-cr alloys, *Scripta Materialia* **59**, 1193 (2008).
- [119] P. Olsson, I. A. Abrikosov, L. Vitos, and J. Wallenius, Ab initio formation energies of fe-cr alloys, *Journal of Nuclear Materials* **321**, 84 (2003).
- [120] D. Nguyen-Manh, P. Ma, M. Y. Lavrentiev, and S. L. Dudarev, Constrained non-collinear magnetism in disordered Fe and FeCr alloys, *Annals of Nuclear Energy* **77**, 246 (2015).
- [121] M. Y. Lavrentiev, K. Mergia, M. Gjoka, D. Nguyen-Manh, G. Apostolopoulos, and S. L. Dudarev, Magnetic cluster expansion simulation and experimental study of high temperature magnetic properties of fe-cr alloys, *Journal of Physics: Condensed Matter* **24**, 326001 (2012).
- [122] T. P. C. Klaver, R. Drautz, and M. W. Finnis, Mag-

- netism and thermodynamics of defect-free fe-cr alloys, *Physical Review B* **74**, 094435 (2006).
- [123] M. Wen, A new interatomic potential describing fe-h and h-h interactions in bcc iron, *Computational Materials Science* **197**, 110640 (2021).
- [124] J. Hou, X. S. Kong, J. J. Sun, Y. W. You, X. B. Wu, C. S. Liu, and J. Song, Hydrogen bubble nucleation by self-clustering: density functional theory and statistical model studies using tungsten as a model system, *Nuclear Fusion* **58**, 096021 (2018).
- [125] J. Hou, X. S. Kong, C. S. Liu, and J. Song, Hydrogen clustering in bcc metals: Atomic origin and strong stress anisotropy, *Acta Materialia* **201**, 23 (2020).
- [126] C. M. Pépin, A. Dewaele, G. Geneste, P. Loubeyre, and M. Mezouar, New iron hydrides under high pressure, *Physical Review Letters* **113**, 265504 (2014).
- [127] J. Badding, R. Hemley, and H. Mao, High-pressure chemistry of hydrogen in metals: In situ study of iron hydride, *Science* **253**, 421 (1991).
- [128] N. Hirao, T. Kondo, E. Ohtani, K. Takemura, and T. Kikegawa, Compression of iron hydride to 80 gpa and hydrogen in the earth's inner core, *Geophysical Research Letters* **31**, L06616 (2004).
- [129] K. Ohsawa, K. Eguchi, H. Watanabe, M. Yamaguchi, and M. Yagi, *Physical Review B* **85**, 094102 (2012).
- [130] M. Myers, P. M. Richards, W. R. Wampler, and F. Besenbacher, *Journal of Nuclear Materials* **165**, 9 (1989).
- [131] Y.-W. You, X.-S. Kong, X.-B. Wu, Q. F. Fang, J.-L. Chen, G.-N. Luo, and C. Liu, *Journal of Nuclear Materials* **433**, 167 (2013).
- [132] E. Hayward, B. Beeler, and C. Deo, *Philosophical Magazine Letters* **92**, 217 (2012).
- [133] P. Olsson, C. Domain, and J. Wallenius, Ab initio study of cr interactions with point defects in bcc fe, *Physical Review B* **75**, 014110 (2007).
- [134] M. J. Puska, R. M. Nieminen, and M. Manninen, Atoms embedded in an electron gas: immersion energies, *Physical Review B* **24**, 3037 (1981).
- [135] Y.-L. Liu, Y. Zhang, H.-B. Zhou, G.-H. Lu, and G. N. Luo, Vacancy trapping mechanism for hydrogen bubble formation in metal, *Physical Review B* **79**, 172103 (2009).
- [136] F. Bozso, G. Ertl, M. Grunze, and M. Weiss, *Applied Surface Science* **1**, 103 (1977).
- [137] M. Weiss, G. Ertl, and F. Nitschke, *Applied Surface Science* **2**, 614 (1979).
- [138] K. Yoshida, *Japanese Journal of Applied Physics* **19**, 1873 (1980).
- [139] R. Imbihl, R. J. Behm, K. Christmann, G. Ertl, and T. Matsushima, *Surface Science* **117**, 257 (1982).
- [140] W. Moritz, R. Imbihl, R. J. Behm, G. Ertl, and T. Matsushima, *Journal of Chemical Physics* **83**, 1959 (1985).
- [141] R. Tran, Z. Xu, B. Radhakrishnan, D. Winston, W. Sun, K. A. Persson, and S. P. Ong, Surface energies of elemental crystals, *Scientific Data* **3**, 160080 (2016).
- [142] K. O. Legg, F. Jona, D. W. Jepson, and P. M. Marcu, Low-energy electron diffraction analysis of clean fe (001), *Journal of Physics C: Solid State Physics* **10**, 937 (1977).
- [143] W. R. Tyson and W. A. Miller, *Surface Science* **62**, 267 (1977).
- [144] M. Ropo, M. Punkkinen, P. Kuopanportti, M. Yasir, S. Granroth, A. Kuronen, and K. Kokko, Oxygen adsorption on (100) surfaces in fe-cr alloys, *Scientific Reports* **11**, 6064 (2021).
- [145] M. Eder, K. Terakura, and J. Hafner, Initial stages of oxidation of (100) and (110) surfaces of iron caused by water, *Physical Review B* **64**, 115426 (2001).
- [146] W. Nichtl-Pecher, J. Gossmann, L. Hammer, K. Heinz, and J. Müller, *Journal of Vacuum Science and Technology A* **10**, 501 (1992).
- [147] L. Hammer, H. Landskron, W. Nichtl-Pecher, A. Fricke, K. Heinz, and K. Müller, *Physical Review B* **47**, 15969 (1993).
- [148] A. Baro and W. Erley, *Surface Science* **112**, L759 (1981).
- [149] J. Krüger, H. D. Kunze, and E. Schürmann, in *Gas and Carbon in Metals* (Springer, New York, 1976) p. 578.
- [150] M. Gupta, R. P. Gupta, and M. Levesque, Effect of surface hydrogen on the anomalous surface segregation behavior of cr in fe-rich fe-cr alloys, *Physical Review B* **86**, 184201 (2012).
- [151] M. Wen, X.-J. Xu, S. Fukuyama, and K. Yokogawa, *Journal of Materials Research* **16**, 3496 (2001).
- [152] P. B. Merrill and R. J. Madix, *Surface Science* **347**, 249 (1996).
- [153] P. Kuopanportti, M. Ropo, D. Holmberg, H. Levämäki, K. Kokko, S. Granroth, and A. Kuronen, Interatomic fe-cr potential for modeling kinetics on fe surfaces, *Computational Materials Science* **203**, 110840 (2022).
- [154] M. Boleininger, S. L. Dudarev, D. R. Mason, and E. Martínez, Volume of a dislocation network, *Phys. Rev. Mater.* **6**, 063601 (2022).
- [155] L. Reali, M. Boleininger, M. R. Gilbert, and S. L. Dudarev, Macroscopic elastic stress and strain produced by irradiation, *Nuclear Fusion* **62**, 016002 (2021).
- [156] Y. Kraftmakher, Equilibrium vacancies and thermophysical properties of metals, *Physics Reports* **299**, 79 (1998).
- [157] X. Li, C. Gao, X. Xiong, Y. Bai, and Y. Su, Hydrogen diffusion in α -fe under an applied 3-axis strain: a quantum manifestation, *International Journal of Hydrogen Energy* **40**, 10340 (2015).
- [158] H.-B. Zhou, S. Jin, Y. Zhang, and G.-H. Lu, Anisotropic strain enhanced hydrogen solubility in bcc metals: The independence on the sign of strain, *Physical Review Letters* **109**, 135502 (2012).
- [159] A. B. Sivak, P. A. Sivak, V. A. Romanov, and V. M. Chernov, Hydrogen diffusion in the elastic fields of dislocations in iron, *Physics of Atomic Nuclei* **79**, 1199 (2016).